2015-09-01

An Improved Dynamic Particle Packing Model for Prediction of the Microstructure in Porous Electrodes

Chien-Wei Chao
Brigham Young University - Provo

An Improved Dynamic Particle Packing Model for Prediction of the Microstructure in Porous Electrodes

Chien-Wei Chao

A thesis submitted to the faculty of
Brigham Young University
in partial fulfillment of the requirements for the degree of

Master of Science

Dean R. Wheeler, Chair
John Harb
Brad C. Bundy

Department of Chemical Engineering

Brigham Young University

September 2015

ABSTRACT

An Improved Dynamic Particle Packing Model for Prediction of the Microstructure in Porous Electrodes

Chien-Wei Chao
Department of Chemical Engineering, BYU
Master of Science

The goal of this work is to develop a model to predict the microstructure of Li-ion batteries, specifically focusing on the cathode component of the batteries. This kind of model has the potential to assist researchers and battery manufacturers who are trying to optimize the capacity, cycle life, and safety of batteries. Two dynamic particle packing (DPP) microstructure models were developed in this work. The first is the DPP1 model, which simulates the final or dried electrode structure by moving spherical particles under periodic boundaries using Newton's laws of motion. The experience derived from developing DPP1 model was beneficial in making the final model, called DPP2. DPP2 is an improved version of DPP1 that includes solvent effects and is used to simulate the slurry-coating, drying, and calendering processes. Two type of properties were used to validate the DPP1 and DPP2 models in this work, although not every property was used with the DPP1 model. First are the structural properties, which include volume fraction, and electronic and ionic conductivities. Experimental structural properties were determined by analyzing 2D cross sectional images of the battery cathodes. These images were taken through focused ion beam (FIB) planarization and scanning electron microscopy (SEM). The second category are the mechanical properties, which include film elasticity and slurry viscosity. These properties were measured through experiments executed by our group.

The DPP2 model was divided into two submodels : active-free and active-composite. The 2D cross sectional images of the simulated structure of the models have a similar particle arrangements as the experimental structures. The submodels show reasonable agreement with the experimental values for liquid and solid mass density, shrink ratio, and elasticity. For the viscosity, both models show shear-thinning behavior, which is a characteristic of slurries. The volume fractions of the simulated structures of the active-free and active-composite models have better agreement with the experimental values, which is also reflected in the 2D cross sectional images of the structure.

Keywords: electrochemistry, structure reconstruction, FIB imaging, LJ potential, granular force

ACKNOWLEDGMENTS

I would like to acknowledge Dr. Wheeler for insightful suggestions and thoughtful discussions, Danilo Bustamante and William Lange for processing images and executing viscosity and elasticity experiments, Medhi Forouzan for running simulations, and my wife, Hannah Han, for support and encouragement. This work was supported by the Batteries for Advanced Transportation Technologies (BATT) program of the U.S. Department of Energy.

Contents

List of Figures

List of Tables

List of Symbols

Roman

A	area
C	carbon
d	diameter
Δs_t	elastic tangential displacement
E	elasticity
F	force
$\mathbf{F}$	force component
$\mathbf{F}_{\mathrm{hz}}$	Hertzian granular pairwise force
I	current
k_B	Boltzmann constant
K	conductivity or elastic constants
L	l*ength*
r	distance
t	time
T	thickness
U	potential energy
v	volume
$\mathbf{v}$	velocity
V	volume fraction
w	weight
W	width
x	fraction of lithium
x_μ	friction coefficient

Greek

γ	damping coefficients
ε	Lennard-Jones energy parameter
ϵ	strain
ϑ	stress
μ	viscosity
ρ	density of an electrode constituent
σ	Lennard-Jones size parameter
τ	shear stress
Φ	Heaviside step function
$\emptyset$	potential field

Subscripts

i,j	domain types
1,2	domain types
c	cathode or cut-off or carbon domain particle
a	active material particle or active material domain
exp	experiment
LJ	Lennard-Jones
LJ/SF	Shifted Force Lennard-Jones
eff	effective
n	normal
t	tangential
gran	granular
l	liquid
s	solid

Superscripts

tot	total

Chapter 1
Introduction

Batteries, one of the families of energy storage technologies, have been used extensively for portable electronics and for emerging applications such as electric vehicles and photovoltaic energy applications. The world's demand for primary batteries (cannot be recharged) and secondary batteries (can be recharged) is estimated to rise 8.5 percent per year to reach $144 billion in 2016 [1]. The growing use of batteries in electric vehicles is motivated by the fact that such systems use energy more efficiently than combustion engines do, even though batteries have much lower specific energy (energy per unit mass) than common fuels such as gasoline [2, 3].

In addition, the rising use of photovoltaic energy applications increases the demand for batteries. Specifically, since electricity generated from a photovoltaic system depends on the intensity of the solar radiation, it is difficult to generate enough electricity at night time or on a cloudy day. However, the use of rechargeable batteries in the photovoltaic system can solve this issue by storing excess electricity when sunlight is strong and supplying energy when the incident radiation is not sufficient to meet the electricity demand.

Li-ion batteries are the most common and highly-used rechargeable batteries [4]. Li-ions move from the anode to the cathode during discharge and back when charging [5]. Mostly due to their high cell voltage (around 4.2 volts), Li-ion batteries offer higher energy density (a product of cell potential and capacity per unit mass) than other types of rechargeable batteries [2]. However, Li-ion batteries still need improvement in the field of electric vehicles and solar energy so that they can exhibit low prices, long cycling life, high specific energy, and safe operation [6-8]. In addition, Li-ion batteries must work at hot and cold temperatures, deliver high power output on demand, and charge quickly [9, 10]. Much work is focused on the development of cost-effective and high-performance Li-ion batteries [11-14].

1.1 Motivation for the work

The power performance of Li-ion batteries partially depends on the resistances in the electrodes. The power represents how much energy is transferred in a certain amount of time. The power obtained from a cell increases by decreasing the internal resistance of the cell. This resistance can be divided into transport (ionic and electronic) and reaction-type resistances. Transport resistances are highly affected by the structure of the electrode, which has led researchers to attempt to optimize the microstructure of electrodes to obtain lower transport resistance [15-18].

Experiments have been done in order to understand the relationship between the microstructure of electrodes and transport resistances. For instance, transport resistance can be minimized by dispersing pores and conductive carbon throughout an electrode [19-21]. Also, transport resistances as a function of porosity (volume fraction of pores) and amount of carbon of a Li-ion cathode were measured through conductivity experiments [22, 23].

Although transport resistances at different constituent volume fractions can be measured through experiments, experiments at every composition level require a lot of time and cost for optimizing electrodes. This problem inspired our research group to create models that can take the place of experiments, since a successful model can require less cost, namely the low cost of computers, to imitate the real system.

Due to the micrometer-scale thickness of electrode films, measuring transport properties is challenging, and results are difficult to interpret because of the confounding effects of multiple physical phenomena. However, an accurate model can determine the fabrication-structure-performance connections in a more fundamental way. An accurate model is capable of virtually investigating transport properties as a function of multiple compositions and conditions.

3D electrode microstructure models have been developed in recent years [24], and have the potential to improve the performance of batteries. A robust 3D microstructure model can be used to predict electrode performance for different manufacturing and design conditions. In addition, a robust 3D microstructure model can be used to find the optimized microstructure of electrodes to lower transport resistance. Two different microstructure models have been used in our research group to study the relationships between electrode microstructure and transport resistances [25].

The first method is the stochastic grid (SG) model [22], which was designed by David Stephenson at BYU. The SG model is based on Monte Carlo (MC) simulation principles [26], which are used to generate the structure of electrodes by swapping voxels, or packets of material. Each voxel contains one of three constituent phases. The grid, a structure that is filled with equal sized cubic voxels, starts as a random distribution of material, and the swap processes continue until the structural statistics of the simulated structure are in best agreement with those for

experimental electrode structure. The SG model is easy to implement in terms of computer code, but at the cost of less realism in describing the natural agglomeration of active material. Also, the SG model cannot simulate the change of a real system during a period of time, like a liquid drying process or the deformation of a solid. Since this project requires a model that can simulate the real system as a function of time, the SG model is not used.

Another method is the dynamic particle packing (DPP) model [25], which was designed by David Stephenson at BYU. The DPP model is a particle-based Lagrangian-type approach where the electrode is simulated by agglomerates of spheres which move collectively under Newton's laws of motion. However, the DPP model was designed to simulate only the microstructure of the finished electrode, rather than the whole fabrication process. This drawback motivates further research into an improved DPP model that can simulate the three main fabrication processes of the electrode, which are slurry-coating, drying, and calendering (rolling press).

1.2 Scope of work

This work is focused on developing a model to simulate the fabrication of the cathode. Specific changes are designed to enable the prediction of slurry viscous behavior, microstructure changes during drying and calendering, and solid mechanical and conductive behavior. This improved model has the potential to assist researchers and battery manufacturers who are trying to optimize batteries for capacity, cycle life, and safety.

To achieve this objective, two models were used in this work. Firstly, the DPP model of Stephenson, which is now called DPP1 model, was applied to imitate the microstructure of the calendered cathode electrode. The DPP1 model was validated by comparing predicted volume

fraction and ionic and electronic conductivities to experimental values. Secondly, the DPP2 model, a new version of the DPP model, was adapted to imitate the full range of wet and dry processing steps for a Li-ion cathode. The DPP2 model was validated by comparing predictions of slurry viscosity, film elasticity, volume fraction, and ionic and electronic conductivities to experimental values. New to this work, LAMMPS [27], a molecular dynamics simulator, was used to run the DPP1 and DPP2 models for the conditions of sphere-based particles.

1.3 Outline

The remainder of this document is organized as follows.

Background.

Chapter 2 is a brief description of the fabrication of li-ion cathode, and 2) the development of battery model.

Cross-sectional imaging and experimental measurements.

Chapter 3 describes the properties that were used to validate the model. Properties such as contact probabilities, tortuosity, ionic tortuosity, and electronic conductivities were obtained from a cross-sectional image of the electrode. Additionally, basic experiments for determining properties such as the slurry viscosity and the elasticity of the electrode are included.

3D microstructure model development and validation.

Chapter 4 reports details and results for the two models, namely the DPP1 and DPP2 models. Both models were validated by comparing predicted properties to experiment and to each other. Chapter 4 concludes with some suggestions for future work to further develop the DPP2 model.

Chapter 2
Background

2.1 Introduction

This chapter provides a basic understanding of Li-ion battery chemistry and the process used to fabricate Li-ion cathodes. Also, the relationship between the microstructure of the electrodes and transport resistance, and an overview of the development of battery models are included. This background is required to better understand the design of the improved DPP model discussed in Chapter 4.

2.2 Li-ion battery chemistry

The electrochemical reactions in a Li-ion battery involve the negative and positive electrodes, with the electrolyte providing a conductive medium for Li ions to move between the electrodes . Figure 2.1 shows a Li-ion battery during charging and discharging. When the battery is discharging, Li^+moves from the negative electrode (anode) to the positive electrode (cathode). When the battery is charging, the reaction goes in reverse. The separator placed between the electrodes is usually a microporous polyolefin film used to prevent physical contact between the anode and cathode [28]. Such contact is called an electrical short and would allow electrons to move directly between electrodes without passing through an external circuit, thus generating

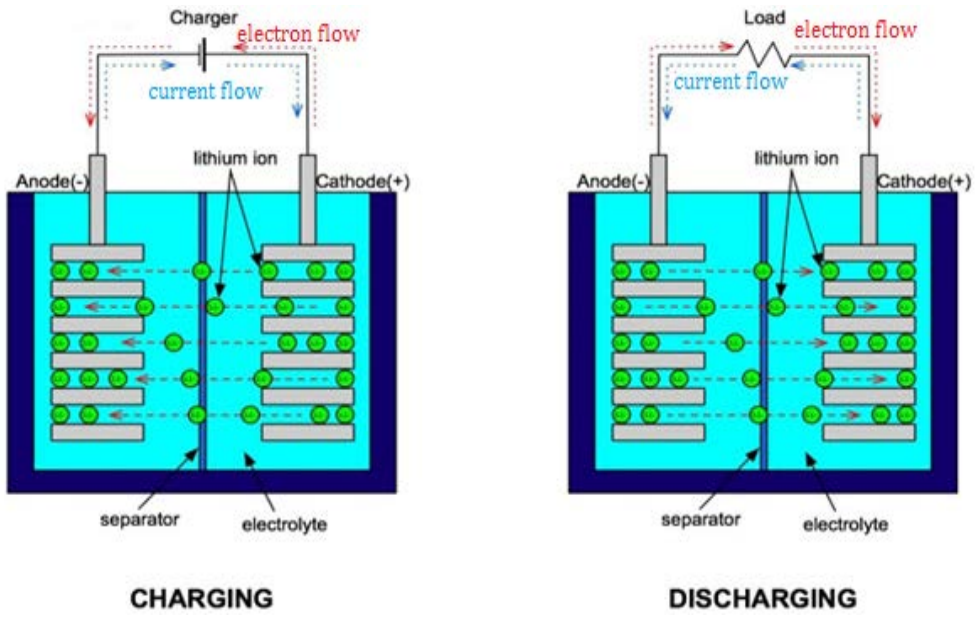

Figure 2.1. Li-ion Charging and Discharging Circuit Diagram [29], used by permission.

heat rather than electrical power. Useful work is generated when electrons flow through the closed external circuit marked as "Load" in Figure 2.1.

In this work, $LiNi_{0.5}Co_{0.2}Mn_{0.3}O_2$ (NCM 523 for short) is the active material of the cathode. The cathode also contains around 5% of carbon black that is added to improve the electronic conductivity [23, 30]. The cathode reaction is

$$Ni_{0.5}Co_{0.2}Mn_{0.3}O_2 + xLi^+ + xe^- \rightleftharpoons Li_xNi_{0.5}Co_{0.2}Mn_{0.3}O_2 \ \text{(cathode)}, \qquad (2.1)$$

where x represents the fraction of lithium and ranges from 0.5 to 1. Although the amount of lithium varies, we write the molecular formula as $LiNi_{0.5}Co_{0.2}Mn_{0.3}O_2$ for convenience.

The anode is typically made up of graphitic carbon because it has a small electrochemical potential versus lithium and it is cheap, lightweight, and electrically conductive [22, 31]. The anode reaction is

$$\mathrm{Li_xC_6} \rightleftharpoons x\mathrm{Li} + \mathrm{C_6} + xe^{-}\ (\mathrm{anode})\,, \qquad (2.2)$$

where C represents the carbon atoms in the solid, and x ranges from 0.5 to 1.

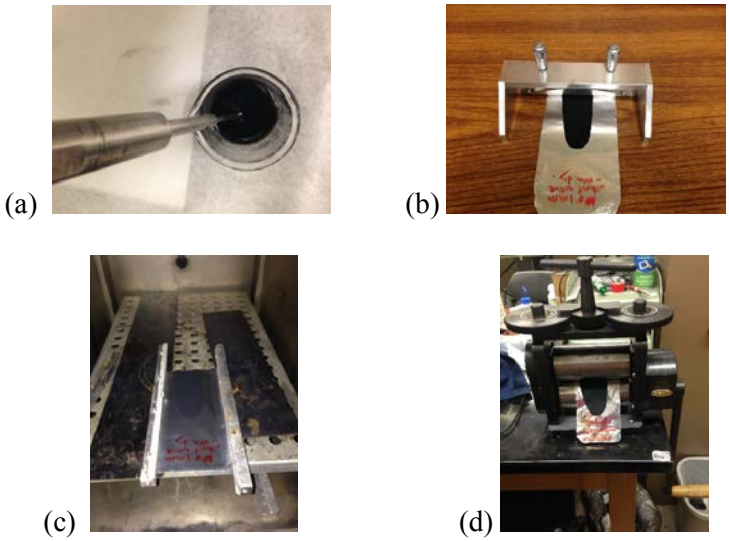

Figure 2.2. Fabrication processes of the battery cathode in laboratory: (a) slurry making, (b) coating, (c) drying in the oven, and (d) calendering.

2.3 Fabrication of a Li-ion cathode

The cathode of a Li-ion battery is composed of active material like NCM and carbon black, bound together by polyvinylidene fluoride (PVDF). Figure 2.2 shows the fabrication of the cathode in the laboratory. Dry cathode materials and a solvent, commonly 1-methyl-2-pyrrolidone fluoride (NMP), are mixed together to form a slurry as shown in Figure 2.2 a. The slurry is placed on a metal foil current collector as shown in Figure 2.2 b, and a doctor-blade is used to smooth the slurry to a uniform film thickness. Then the film is placed into an oven to evaporate the solvent (NMP) under vacuum. After drying, the film is taken out of the oven as shown in Figure 2.2 c and run through a calendering machine, which is a set of closely spaced metal rollers, to achieve the desired thickness and porosity as shown in Figure 2.2 d.

The industrial cathode fabrication process is similar to the laboratory process except the following. (1) The mixer is much larger to contain more slurry as shown in Figure 2.3 a. (2) The slurry is applied onto a continuous roll of metal foil current collector using a coating machine as shown in Figure 2.3 b. (3) The thickness of the slurry film is controlled through a large size doctor-blade or a slot die as shown in Figure 2.3 c. And (4) the roll containing the film passes into an oven to cure and the dried film is then passed through a calendering machine to compress as shown in Figure 2.3 parts d and e.

Figure 2.4 a shows an SEM cross section of a calendered cathode. The image shows that this particular active material exists as large, approximately spherical particles while pores and carbon are dispersed throughout the cathode. The carbon black particle size is around 50-100 nm. These carbon particles form many large domains or aggregates caused by strong interaction with the binder, which glues the carbon black together as well as adheres the carbon black to the active material particles. In addition, nano-pores appear in the carbon/binder mixture when the solvent evaporates during the drying process. On the other hand, macro-pores generally appear next to the active material particles. The reason for this could be that the binder does not completely adhere the carbon black to the active material particles, leaving the macro-pores around them when the solvent evaporates. These macro-pores remain in the cathode even after the calendering process takes place.

The aim of this work is to simulate the fabrication process of the cathode and generate a structure that closely matches the experimental structure of the final cathode. Figure 2.4 b shows the cathode image after computer processing (image segmentation) to highlight the active material (blue), carbon domains (green), and pores (white). What we term the carbon domain is actually a mixture of carbon black, binder, and nano-pores. For convenience in segmenting

images and reducing modeling cost this mixture is approximated as a uniform carbon domain. The details of the model and the comparison to the cross section images are discussed in Chapters 3 and 4.

(a)  (b)  (c) 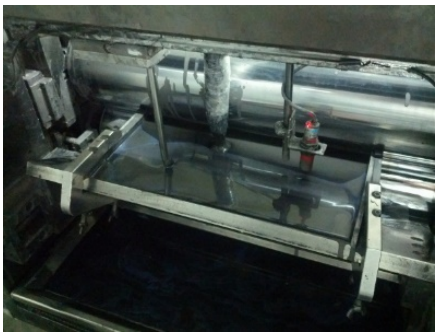

(d)  (e) 

Figure 2.3. Fabrication processes of the battery cathode in industry [32], used by permission. (a) A mixer used to mix dry material with solvent (b) A coating machine used to coat slurry on current collectors. (c) A doctor-blade used to control the thickness of the coated slurry on current collectors. (d) An oven used to cure the slurry. (e) A calendering machine used to make the electrode thinner.

(a) 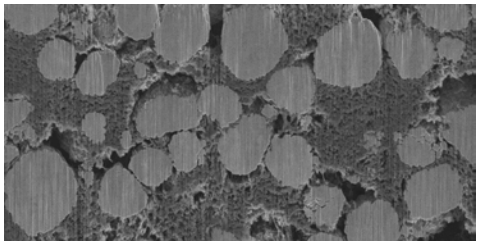 (b) 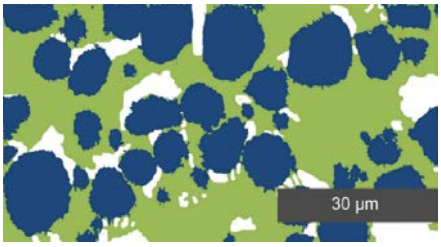

Figure 2.4. FIB/SEM images of electrode films at 30% porosity. (a) Original image (b) Segmented image. Blue represents active material domains, green represents carbon domains, and white represents macro-pore domains, respectively.

2.4 Microstructure and transport processes

A typical Li-ion electrode is composed of active material, carbon black, binder, and pores (Figure 2.4). During discharge, the electrons move from the anode (negative electrode) to the cathode (positive electrode) through the current collector located on each electrode (Figure 2.1). The ions move from the anode to the separator and then to the cathode through the electrolyte. The electrochemical reaction happens when electrons and ions meet on the surface of active particles.

Battery performance is partially dependent on the electronic and ionic transport resistances [33]. Active material for cathodes generally has low electronic conductivity. For instance, the conductivity of $LiCoO_2$ is around 10^{-4} S cm^{-1} while the conductivity of the aluminum current collector is around $3.4 \cdot 10^5$ S cm^{-1} [34]. A small amount of carbon black added into the cathode can increase the effective electronic conductivity of the composite. This occurs because the carbon black forms electronically conductive pathways between active material particles. Likewise, the ionic conductivity can be increased by having more pores near the surface of the cathode film contacting the electrolyte so that more ions can move into the electrode [35]. Generally, to have low electronic and ionic transport resistances requires that pores and conductive carbon be dispersed throughout the electrode [19, 20, 30].

The processes for lowering electronic and ionic resistances are competing processes. When more conductive carbon is added into the cathode, large carbon domains form (as shown in Figure 2.4b). As these carbon domains become larger they occupy the pore spaces and reduce the pathways for ion transport—effectively increasing the ionic transport resistance. Conversely, if the carbon domain size is reduced, ionic transport becomes easier at the expense of electronic transport [35]. In addition, the calendering process can also affect the electronic and ionic

resistances. In calendering the porosity of a film and the separation distances between particles are decreased. The result is increased ionic transport resistance and decreased electronic resistance. In order to balance ionic and electronic transport and the best battery performance, the microstructure must be optimized. This optimization can be aided by the use of microstructure modeling.

2.5 Macro-level model development

Macro-level battery models use averaged parameters to represent the influence of microstructure on porous electrode transport phenomena. The most renowned analytical model was developed by Newman and coworkers [36, 37] for predicting battery behavior. The Newman model is based on one-dimensional transport across battery components with assumptions that the electrode is an isotropic, homogeneous, porous material constructed from mono-disperse (uniform size) spherical particles. These simplifications decrease numerical computation costs greatly. Although this 1D model can predict some aspects of battery performances from design parameters (such as film thickness and porosity) [24], they require and cannot predict effective transport properties, due to the fundamental lack of microscopic detail. Therefore, either extensive experiments or a predictive 3D microstructure model is required to obtain effective (total volumetrically averaged) transport parameters.

2.6 Microstructure model development

3D non-predictive model.

3D microstructure models can be categorized into non-predictive and predictive models. Many researchers have worked on non-predictive models to reconstruct 3D electrodes and

analyze their 3D microstructures [38-40]. Sastry and coworkers explored models based on a random packing of spherical or ellipsoidal particles [15, 16]. Siddique and Liu proposed a model that uses random seeding and growth of particles in order to generate 3D structures [17]. Awarke et al. used a dynamic collision algorithm to produce a 3D mesoscale model of the collector-electrode interface in Li-ion batteries [41]. Finally, K. Rhazaoui et al. designed 3D model to determine the effective conductivity of solid oxide fuel cell electrodes [42].

Recently, models have also been developed that combine 3D microstructure models with electrochemical models. Hutzenlaub and coworkers developed a model that coupled microstructure of a $LiCoO_2$ battery cathode with electrochemistry to study the electric potential and lithium/salt concentration distribution in both the liquid electrolyte and solid active-material phases [43]. Scott and coworkers developed a model that combined mechanical and electrochemical simulations to study the mechanical degradation of the $LiCoO_2$ cathode electrode for capacity fade [44]. The model includes swelling, deformation, and stress generation driven by lithium intercalation.

In summary, these models can provide information such as effective conductivity or Li concentrations during discharging from the 3D microstructure, but the models cannot predict the microstructure behavior for different porosity or different active materials. This motivated the development of 3D predictive models by our group at BYU.

3D predictive model.

Few groups have used predictive models to generate the microstructure of electrodes. For example, our group developed 3D microstructure models to study the relationships between

electrode microstructure and ionic transport resistances of Li-ion and alkaline battery cathodes [25, 45].

As described in Chapter 1, two predictive models were developed by our group, namely, stochastic grid (SG) model and the dynamic particle packing (DPP) model. Since the aim of this is to improve the DPP model, the details of the DPP model and new algorithms added to improve the DPP model are discussed in Chapter 4.

Chapter 3
Cross-sectional imaging and experimental measurements

3.1 Introduction

Simulation models are imitations of the operation of a real-world process or system, and they never exactly describe the real-world system [46]. Due to that, a model should be verified and validated to the degree needed for the model's intended purpose or application [47]. Validation of a model usually is executed by comparing properties generated from the model and measured from experiments.

Table 3.1 shows two types of properties that were used to validate the DPP1 and DPP2 models in this work, though not every property was used with each model. First are the structural properties, which include volume fractions, electronic and ionic conductivities, and the changes in overall volume upon drying. Experimental structural properties were determined by analyzing 2D cross section images of the battery cathodes. These images were taken through focused ion beam (FIB) planarization and scanning electron microscopy (SEM).

Table 3.1. Properties used for validating the model.

Structural properties	Domain volume fractions
	Electronic and ionic conductivities
	Shrink ratio and densities
Mechanical properties	Film elasticity
	Slurry viscosity

The second category are the mechanical properties, which includes film elasticity and slurry viscosity. These properties were measured through experiments executed by our group. Structural properties are useful validation tools for the DPP1 and DPP2 models because an accurate microstructure will enable the model to predict the other electrode properties of interest. Mechanical properties are important for the DPP2 model because they are relatively easy to measure and relate to electrode behavior during the fabrication process of the electrode, including slurry-coating, drying, and calendering.

This chapter describes how the 2D cross section images of electrodes are obtained and how those images are processed to obtain structural properties. We then present experimental methods to determine mechanical properties. The imaging and experiments were performed on commercially made NCM cathode slurries and films.

3.2 Experimental electrodes

Three types of cathode films are examined in this study: finished cathode, uncalendered cathode, and uncalendered cathode which doesn't contain active material (called "active-free film"). The composition of these films are shown in Table 3.2. The finished cathode films were sent from Argonne National Lab. Material properties of the finished NCM cathode can be found in Ref. [48]. The properties obtained from the finished cathode film were used to validate DPP1 model.

The uncalendered cathode and uncalendered active-free films were made by our group using materials provided by Argonne National Lab. The uncalendered active-free film was used to develop the prototype of DPP2 model, since DPP2 model is more complicated than DPP1

model. Properties obtained for these two uncalendered cathode films were used to validate DPP2 model.

For some elasticity experiments, the aluminum current collector was taken off the cathode films. To do that, melted gallium was put on the surface of the cathode film so that gallium can remove the current collector. More details are explained in Ref [23]. The fabrication of uncalendered cathodes is based on previous work [23, 49], except the PVDF was pre-dissolved in NMP solution, in contrast to the prior procedure. The fabrication of the uncalendered active-free film uses the same process as normal uncalendered cathodes, except active material was not used. The fabrication process is as follows: (1) Mix active material NCM (Argonne National Lab) and carbon black (Denka Carbon, Argonne National Lab) with mortar and pestle for 20 minutes. (2) Add the dry NCM/carbon black mixture to a PVDF-NMP solution (contains 8% wt of PVDF, provided by Argonne National Lab). (3) Add additional NMP solvent to the NCM/carbon black/PVDF/NMP solution to achieve the desired mount of NMP (see Table 3.2). (4) Stir the mixture with an ultrasonic homogenizer for 20 minutes to form a slurry. (5) Cut an aluminum current collector (25 μm thick) into 20 cm × 20 cm and place it on a glass plate. (6) Put a few drops of alcohol on the current collector and use a glass roller to smooth the current

Table 3.2. The composition of films.

	Solid (dry wt%)			Added NMP (g/100 g solid)
	NCM	PVDF	Carbon Black	
Finished Cathode	90	5	5	92.5
Uncalendered Cathode	90	5	5	92.5
Uncalendered Active-Free film	0	50	50	92.5

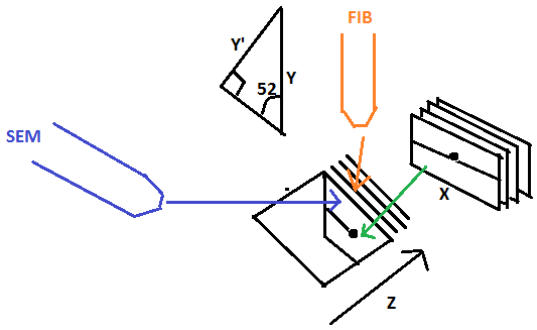

Figure 3.1. Schematic diagram of relative sample and beam orientations in a dual beam FIB instrument.

collector. (7) Apply the slurry to the current collector, and use a doctor blade (Byk-Gardner,U.S.A) to adjust the coating thickness to 175 μm (it is 200 μm including current collector). (8) Dry the slurry film in a vacuum oven (120℃; 3 kPa absolute) for 12 hours. (9) Cut the dry film into multiple 22 mm × 22 mm cathode samples.

3.3 Characterize structure through FIB/SEM imaging

Characterizing the microstructure of a material in this work starts by producing a series of 2D slice images of the cathodes, and obtaining properties by analyzing these 2D images. Focused ion beam (FIB) / scanning electron microscopy (SEM) is used to make this cross-section process possible and easier for image analysis. Figure 3.1 shows that focused ion beam can mill away and create segmental cross sections of the material, then the SEM can take a snapshot of each cross section. The whole set of images can be processed to measure the structural properties, and compared with the results from simulation. In this work, imaging was done by our group with a dual-beam FIB/SEM instrument at BYU. These 2D cross-section images are pre-processed through image alignment, stretching, cropping and segmentation as discussed below.

Image alignment.

When the images are milled away, the focused ion beam moves in the *z* direction at a constant step size (Figure 3.1). Hence, the distance between the SEM camera and *xy* plane of the cathode increases as the ion beam cuts deeper into the cathode. Over time this movement slightly misaligns the images obtained by the camera. Thus, even though the SEM can self-adjust the position to align the images, a misalignment between images still exists and must be corrected. To accomplish this correction, the stack of SEM/FIB 2D images are aligned together using a Matlab code provided to us by the porous media group at IMTEK/University of Freiburg. An unmilled area which does not change much from image to image was chosen as a reference point to help correct the alignment of the entire image stack.

Image stretching.

The 2D images taken from SEM require another correction in *y* direction because the SEM took images at an angle that is not perpendicular to the *xy* plane. As shown in Figure 3.1, the relationship between the original image (Y') and corrected image (Y) in the *y* direction is

$$Y = \frac{Y'}{\sin(52°)}, \tag{3.1}$$

Hence, each image in the stack needs to be stretched 1.27 times in *y* direction.

Image cropping and segmentation.

As can be seen in Figure 3.2 a, d, and g, some areas of these images are unnecessary because they cannot be used to obtain properties of the electrodes for comparison with model results. Images are cropped by using the ImageJ software to remove the fringes. The cropped images are shown in Figure 3.2 b, e, and h. After cropping, the images are segmented manually

by using Photoshop to identify the intensity of each phase. Segmented images for three different cathode samples are shown here as Figure 3.2 c, f, and i.

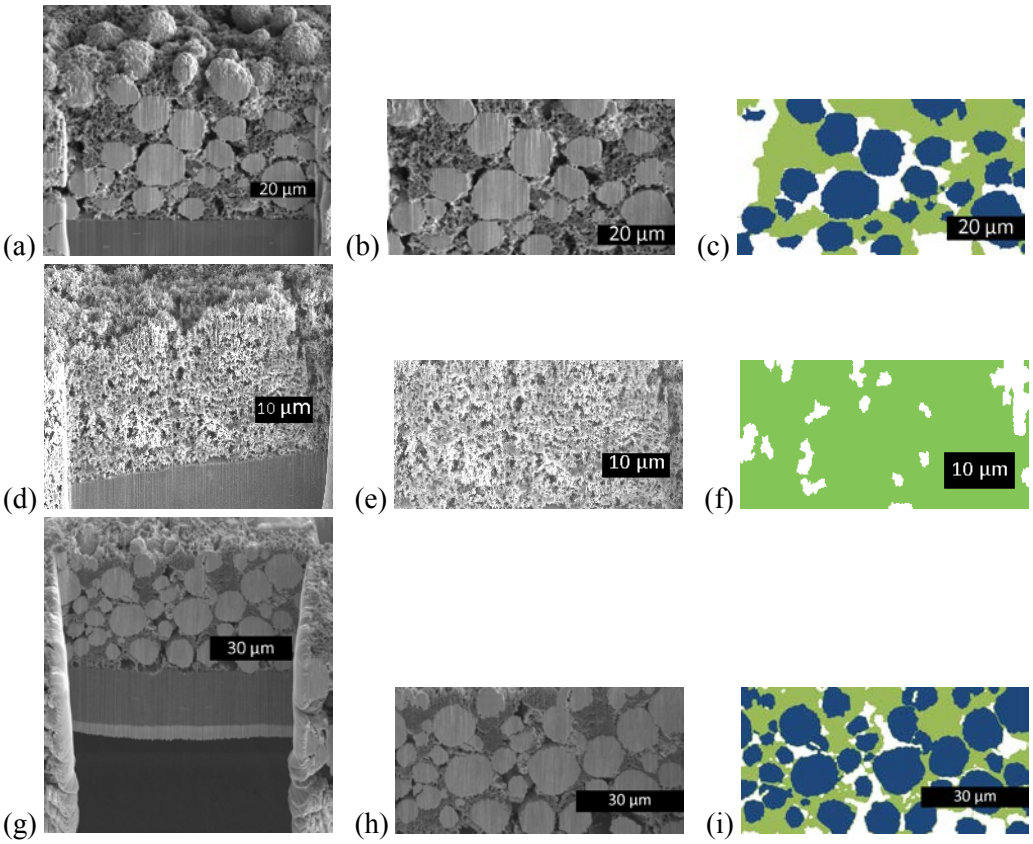

Figure 3.2. FIB/SEM images of three cathode electrode films. (a) Uncropped image of uncalendered electrode film. (b) Cropped image of uncalendered electrode film. (c) Segmented image of uncalendered electrode film. (d) Uncropped image of uncalendered active-free electrode film. (e) Cropped image of uncalendered active-free electrode film. (f) Segmented image of uncalendered active-free electrode film. (g) Uncropped image of finished electrode film. (h) Cropped image of finished electrode film. (i) Segmented image of finished electrode film.

3.4 Structural properties

3.4.1 Volume fraction

Volume fraction is a basic property used to validate the model. The volume fraction of each constituent can be calculated from a traditional method based on the macroscopic

measurements of the mass and density [45]. The method is described as follows. The volume of a cathode film is $V_c = L_c\, W_c\, T_c$, where L_c is the length of the film, W_c is the width of the film, and T_c is the thickness of the film. The volume fraction of active material, carbon black, and binder is

$$\mathrm{V}_i = \frac{w_i}{\rho_i V_c}, \tag{3.1}$$

Where w_i is the weight of the dry material i, and ρ_i is the density of the dry material. The volume fraction of pores (called porosity) is

$$\mathrm{V}_{\text{pores}} = 1 - \mathrm{V}_{\text{active material}} - \mathrm{V}_{\text{carbon black}} - \mathrm{V}_{\text{binder}}\,. \tag{3.2}$$

As described in Section 2.3, carbon black, binder, and nano-pores are treated as a homogeneous domain for convenience in segmenting SEM images and in reducing modeling cost. By doing that, active material, carbon domains, and macro-pores are the only domains or phases in the images of simulated cathodes from the DPP1 and DPP2 models. Thus, the experimentally determined volume fraction of each constituent cannot be compared with the volume fraction of each domain from the models unless the volume fraction of nano-pores for the carbon domain is known. The relationship of volume fraction between the cathode and models is shown in Figure 3.3.

In order to determine the volume fraction of nano-pores in the carbon domain, it is estimated from the total porosity of a cathode that does not have active material (active-free). This assumption is based on previous work that showed that great majority of the pores in the active-material-free cathode are only nano-pores [22]. Hence, the volume fraction of the carbon domain can be obtained by adding the volume fractions of carbon black, binder, and nano-pores.

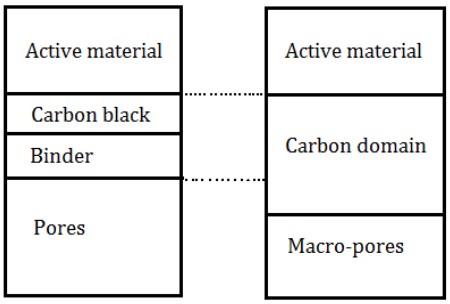

Figure 3.3. Relationship of volume fractions between actual cathode and microstructure models.

The second method to calculate the volume fraction is done by counting the relative number of pixels/voxels of the 2D segmented images (see Figure 3.2). In this work, the second method was used to obtain the volume fraction of each domain in the test cathode because of its simplicity compared to the first method. The volume fraction of electrodes was obtained by running a built-in program in Matlab (imread) to transfer image to domain identities (active material, macro-pore, and carbon) according to its colors.

3.4.2 Computation of electronic and ionic conductivities of 3d cathodes

In this work, we use a conductivity model to compute the electronic and ionic conductivities of the 3D FIB/SEM structures instead of experimentally measuring the conductivities of the cathode film. Because the same algorithm can apply to the DPP1 and DPP2 models, results from FIB/SEM structures and simulations can be compared to validate the models, even if the exact conductivities are not correct. This conductivity model requires reasonable values of the intrinsic domain conductivities, which are the conductivities of domains such as active material, carbon domain, and macro-pores. Here, we adapted the values of intrinsic particle conductivity from Ref. [22] , as shown in Table 3.3.

Table 3.3. Domain conductivities of Li-ion battery components: Active material, Carbon domain, and Macro-Pores.

	Active material	Carbon domain	Macro-Pore
Electronic conductivity ($S\ m^{-1}$)	1	500	0
Ionic conductivity ($S\ m^{-1}$)	0	50	1000

The conductivity model uses the finite volume method [38] and periodic boundary conditions to compute the electronic and ionic conductivities of the 3D structures. In the beginning, an external potential gradient $\nabla\emptyset^{\text{ext}}$ is imposed across one dimension of the 3D grid structure. Then current flows between voxels are calculated, to be used in the conservation law, namely that all current flows into one voxel should sum to zero. This creates *N* equations for the unknown potential at each of *N* nodes. These potentials are solved iteratively. The current flows are then summed to a total current I^{tot} at multiple planes perpendicular to the flow of $\nabla\emptyset^{\text{ext}}$. I^{tot} at the middle and end planes were compared for convergence, and the model reminders user the difference in I^{tot} between the middle and end planes if the difference is greater than 5%. The conductivity is computed by the following formula

$$K^{\text{eff}} = \frac{I^{\text{totavg}}}{A|\nabla\emptyset^{\text{ext}}|}\ , \tag{3.1}$$

where K^{eff} is the effective conductivity such as ionic or electronic conductivity, *A* is the cross section of the plane, I^{totavg} is the average of I^{tot} at the middle and end planes and is a function of intrinsic conductivity. The details of this conductivity model can be found in Ref. [45].

(a) 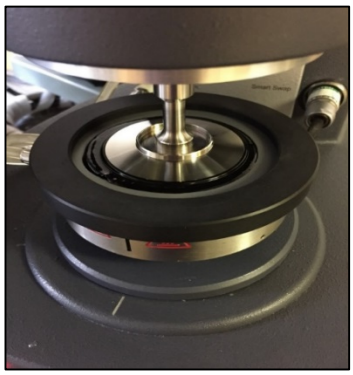 (b) 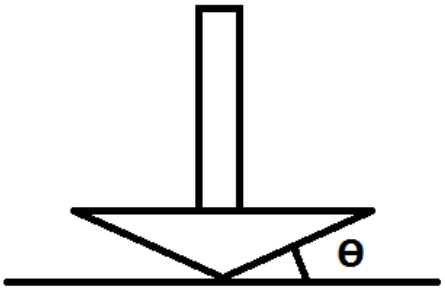

Figure 3.4 (a) Cone/Plate Viscometer (b) Cone/Plate.

3.5 Mechanical properties

3.5.1 Determination of the experimental viscosity of slurries

Viscosities of slurries were measured by our group using a cone/plate viscometer (TA Instruments) at BYU. The principle of this viscometer is that the force required to turn an object in a fluid, is related to the viscosity of that fluid. As showed in Figure 3.4, a cone of very shallow angle is in contact with a stationary flat plate. The cone rotates at a known speed. Using the rotational speed and the power input, the torque can be found and used to calculate the viscosity of the fluid. With this system the shear rate beneath the plate is constant to a reasonable degree of precision, and a graph of shear stress (torque) against shear rate (angular velocity) yields the viscosity. Notably, the viscosity of the active-free slurry was measured through a cone, while the viscosity of the cathode slurry was measured through a plate because the hardness of the active material particles can damage the surface of the cone.

Since the aim of the DPP2 model is to simulate the fabrication of cathodes in industry, it is required to know the shear rate corresponding to the viscosity of the slurry when the slurry passes under a doctor blade. Based on discussion with battery fabricators and by viewing videos of coating processes, we estimated the range of coating speeds to be 1 to 10 $m \cdot min^{-1}$. For our

baseline material (NCM active material and carbon black), the slurry is coated to thickness 175 μm. Taking the ratio of these two quantities gives a shear rate of approximately 100 to 1000 s^{-1}.

In this work, the measurements of viscosity were executed at different shear rates ranging from 1 to 1000 s^{-1} at 25℃ for cathode slurry and active-free slurry. The plot of viscosity at different shear rates is shown in Chapter 4 where it is compared with simulation results, which are likewise described.

(a)  (b) 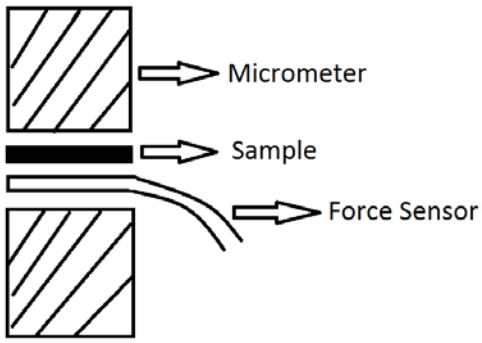

Figure 3.5. (a) Equipment used to measure the vertical elasticity of samples. (b) Schematic of the equipment (not to scale).

3.5.2 Determination of the experimental elasticity of the uncalendered cathode films

As described above, elasticity of the cathode film can give an insight to the solid behavior during the fabrication process of the electrode. To measure the elasticity of the uncalendered cathode films a force is applied to compress them. However, due to the fragile and thin nature (thicknesses are around 40-60 μm) of cathode films, it is difficult to apply and measure the required stress and strain when using a standard stress/strain apparatus. For example, the minimum force generated from the Instron apparatus used at BYU for small materials is 2 kN. Even the minimum force generated from the mini Instron apparatus, which is designed for small

materials, is 0.5 kN. This force is enough to destroy cathode films. Furthermore, the minimum movement of the Instron and mini Instron apparatuses are 0.25 mm and 0.05 mm respectively, which are longer than the thicknesses of cathode films. This means these apparatuses cannot detect minute changes in the strain of cathode films. Hence, our research group designed vertical elasticity measurement equipment that generates a minute force to compress these cathode films without destroying them. This equipment is composed of a Force sensor (FlexiForce® Sensor-25lb), micrometer (Chicago brand P.N. 50059), Digital multimeter (Agilent 34410A), and a generic clamp. The set-up is shown in Figure 3.5.

In the beginning of the experiment, the force sensor was calibrated as instructed by the manufacturer, confirming that conductance of the probe is linearly related to the force being applied. The results of the calibration experiment were used to calculate force applied by micrometer, and the micrometer was used to measure changes in thickness. The force probe and sample were placed between the anvil and spindle of the micrometer, and the sample and probe were pressed until the ratchet screw clicked. At this point initial thickness and force was measured. Following this, the cathode was compressed further while making additional thickness and force readings. Elasticity (E) or Young's modulus is defined by a linear relationship between strain (ϵ) and stress (ϑ): $E = \frac{\vartheta}{\epsilon}$. Stress is calculated from $\vartheta = \frac{F}{A}$, where F is the force measured by the probe and A is the micrometer anvil surface area ($2.327\ \mathrm{cm}^2$). Strain was calculated by $\epsilon = \frac{(l_0 - l)}{l_0}$), which is the change of sample thickness divided by initial thickness. Elasticity results of uncalendered active-free film and uncalendered cathode film are compared with simulation results in Chapter 4. Figure 3.6 is the plot of stress and strain of the uncalendered active-free film and uncalendered cathode film. Slopes made from strain points less than 0.05 for uncalendered active-free film and 0.04 for uncalendered cathode film were used to determine elasticity by a

least squares procedure. Permanent or plastic deformation [50] occurs at large stress values, causing the points to form a nonlinear curve.

3.6 Conclusion

This chapter discussed two types of properties used to validate the DPP1 and DPP2 models. The first type involves structural properties, which include volume fraction and ionic and electronic conductivities. An additional structural property known as the shrink ratio is defined and used in Chapter 4. Structural properties are important for DPP1 and DPP2 because an accurate microstructure will enable the model to predict the other electrode properties of interest. The second type of properties are mechanical properties, which include slurry viscosity and film elasticity. Mechanical properties are used to evaluate the DPP2 model because they relate to electrode behavior during the fabrication process of the electrode, including slurry-coating, drying, and calendering, while still being relatively easy to measure.

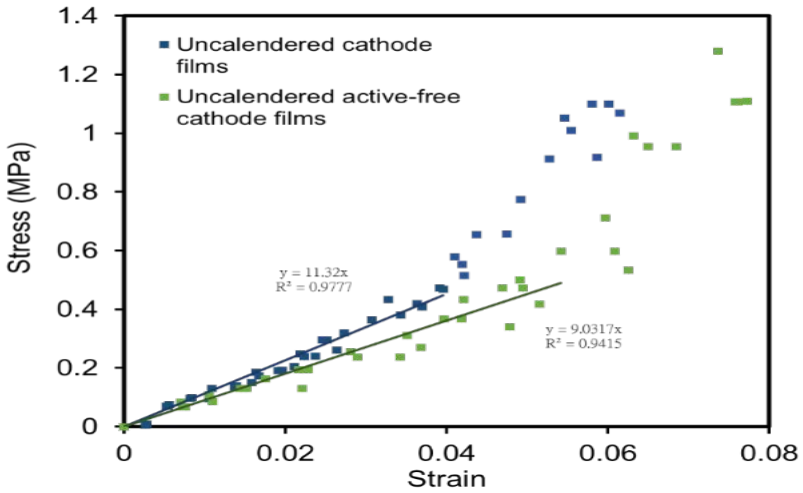

Figure 3.6. Stress versus strain during the compression of uncalendered cathode films (blue points), and calendered active-free films (green points). For each type, three independent films were tested within the aggregate set of points. The lines show least-squares fits to the linear regions.

Chapter 4
3D microstructure model development and validation

4.1 Introduction

In the past, not much was understood about how the particles behave during the slurry-making, drying and calendering processes and how the movement and organization of particles affect final cell performance. This led us to develop a new model that can simulate these processes. The long-term goal in developing this new model is to allow us to understand what fabrication conditions can create an optimal structure for best performance.

Two microstructure models were developed in this work, as introduced in Chapter 1. The first is DPP1, which simulates the final or dried electrode structure by moving spherical particles under periodic boundaries and Newton's laws of motion. The second is the DPP2 model, an improved version of the DPP1 model adapted to imitate the full range of wet and dry processing steps for a Li-ion cathode The experience derived from developing the DPP1 model was beneficial in making the DPP2 model, since the DPP2 model is more complicated than the DPP1 model.

This chapter reports results for the DPP1 model and the development and results for the DPP2 model, including the design principles, simulation tools, and operation procedures. Both

models were validated by comparing simulated properties to experiment properties; DPP1 model was validated by comparing structural properties, and DPP2 model was validated by comparing structural and mechanical properties.

4.2 Number of particles in the model

The computational cost is too high if all electrode components are included in the model separately. For example, the explicit solvent molecules are less than 1 nm, the explicit binder molecules (polymer) are similarly small, the diameter of carbon black is 50-100 nm, and the diameter of active material is 1-15 μm. Even if solvent and binder molecules are excluded, leaving only carbon black and active material particles, it is estimated that at least 10^6 particles would be needed to simulate an electrode with thickness 30-200 μm. However, this would require several months of computing time to obtain results from one simulation when using the BYU supercomputing resources. To minimize the computational cost the smaller molecules and particles (solvent, binder, and carbon) were lumped together into "carbon domain" particles to reduce the total number of particles in the final model to around 5500, leading to simulations that required about 1 day of computing time.

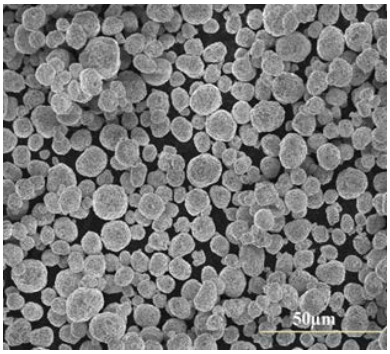

Figure 4.1. Pristine NCM particles deposited on a surface and imaged through SEM.

4.3 Active material size distribution in the model

In addition to combining non-active material components together, the distribution of active material sizes was also simplified. In manufactured electrodes, active material particle sizes fall under a continuous size distribution (see Figure 4.1). Instead of attempting to replicate every particle size, this distribution was simplified into a series of discrete particle sizes. An experimental particle-size distribution was collected by measuring 249 active material particles ranging from 0.8 to 15 μm that could be isolated from a series of SEM 2D slice images for one cathode sample. The size of each active material particle was obtained by first finding the 2D slice image where that particle's cross sectional area was greatest (close to the particle's midpoint in the *z* direction). Then, the two longest-possible perpendicular lines or chords were drawn on each particle and were measured. A geometric average of these two lines was then used to calculate an average diameter for the particle (See Figure 4.2). The resulting distribution of diameters is shown in Figure 4.3 in coarse-grained form.

The procedure for picking the active material particle sizes used in the model is as follows. The particle size distribution was first divided into bins for different size intervals. It was found in the previous DPP model by Stephenson that spacing these intervals approximately equally according to volume fractions gave the best results [51]. The representative single particle size for each bin and the number of particles in the bin were chosen to conserve the total volume and total surface area of the particles in that bin. The formulas used to accomplish this can be found in Ref. [51]. Table 4.1 contains the model active material particle sizes $d_{a,\mathrm{exp}}$, the volume fractions used in the models, and the relative number of particles.

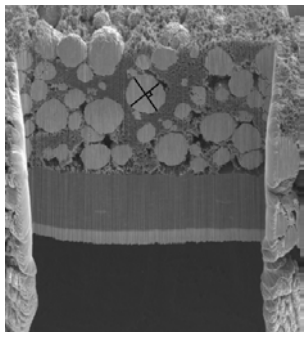

Figure 4.2. Demonstration of determining the size of active material particle, showing two original chords that lead to an average diameter.

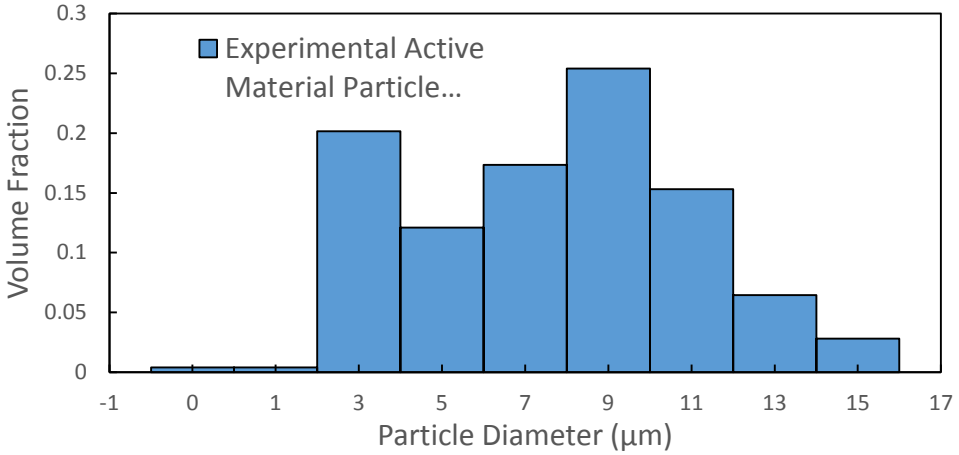

Figure 4.3. Experimental particle size distribution of NCM.

Table 4.1. NCM eight model active material particle sizes, volume fractions, and relative number of particles.

$d_{a,\mathrm{exp}}$ (µm)	Volume fraction	Relative number of particles
0.724	0.0040	0.3119
2.147	0.2016	0.5984
4.207	0.1210	0.0478
6.171	0.1734	0.0217
8.074	0.2540	0.0142
9.952	0.1532	0.0046
11.563	0.0645	0.0012
15.264	0.0282	0.0002

4.4 Particle simulator

In this work, the DPP1 and DPP2 models were implemented in LAMMPS (Large-scale Atomic/Molecular Massively Parallel Simulator), a classical molecular and granular dynamics code [27]. LAMMPS can be used to model atomic, molecular, and mesoscale systems including soft materials (biomolecules, polymers), and solid-state materials (metals, semiconductors). LAMMPS is designed to be flexible in terms of the number of processors used and was run on the BYU supercomputers. All the features used in this work were controlled by changing the input text files.

LAMMPS requires specific input files to compute properties of the simulated box, a confined space for the simulation of particle interactions, such as viscosity, thermal conductivity, and elasticity. In this work, viscosity and elasticity computation methods were adapted for DPP2 validation. The viscosity and elasticity computation methods are discussed as follows.

Viscosity

The shear viscosity of a fluid is a measure of its resistance to deformation by shear stress. More specifically, it is the transfer of momentum in a direction perpendicular to the velocity. The equation defining shear viscosity is

$$\tau = -\mu \frac{\partial u}{\partial y} \quad , \tag{4.11}$$

where τ is shear stress (the momentum flux) in units of momentum per area per time, $\frac{\partial u}{\partial y}$ is the spatial gradient of the velocity of the fluid moving in the direction normal to the area through which the momentum flows, and μ is the viscosity of a fluid with units of pressure-time.

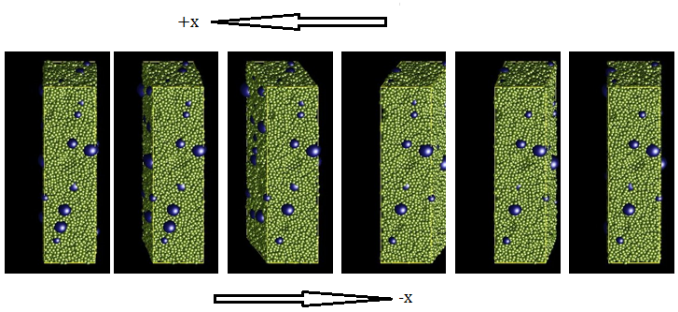

Figure 4.4. The process of viscosity computation through NEMD.

The shear viscosity of the DPP2 model was measured through performing a non-equilibrium MD (NEMD) simulation by shearing the simulation box at a specific rate. As shown in Figure 4.4, the simulated box is sheared in the *xy* plane. Because this simulation has periodic boundaries, when the box is sheared to one side, the edge of the box being sheared reappears on the other side when the box is tilted to 45°. During this time the velocity profile and stress tensor are monitored. Averages of these properties are used to determine viscosity with the above equation. Additional details of the NEMD method can be found in Ref. [52]

Elasticity

Elastic constant is the measure of the stiffness of a material. The elastic constant of the model was estimated by deforming the simulation box in one direction in a constant length change and measuring the change in the stress tensor, which is shown in Figure 4.5. In this work, the elasticity in *z* direction is computed because the elasticity of the cathode films were also measured in *z* direction.

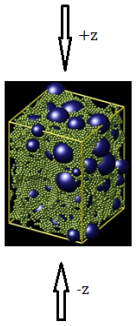

Figure 4.5. Elastic constant computation of the model.

4.5 DPP1 model

The DPP1 model was developed to imitate the micro-scale arrangement of active material particles, carbon domain particles (carbon + binder+ nano-pores), and macro-pores, based on agglomerates of overlapping spheres inside a fixed volume representing a portion of a finished electrode [53]. The advantage of DPP1 model is the simplicity of the parameters. The model applies a Lennard-Jones interaction potential between particles, and using Newtonian mechanics generates a simulated configuration of the final electrode. Two parameters are required in the Lennard-Jones potential function: σ and ε, which represent the size of the particle and the attractive energy well depth, respectively.

In this work a Shifted Force Lennard-Jones (LJ/SF) potential [54] is used instead of a standard Lennard-Jones (LJ) potential [55]. LJ-type potentials have been used for many decades in particle simulations because they are fast to compute and capture the essential physics of decreasing attraction between particles at large separation distance and repulsion between particles at short separation distance. The present model is designed to simulate the particle interactions on a micro-scale instead of a sub-nano-scale associated with typical molecular dynamics simulations. This means that only short-range interactions (compared to particle sizes) between particles are considered. The cut-off distance is the separation distance beyond which

the potential and force are taken to be zero, which is used in virtually all particle-based simulations in order to reduce computational cost. However, there should be minimal discontinuity in the force and potential at the cut-off distance. The standard LJ potential usually has a large ($r_c \approx 3\,\sigma$) cut-off distance which, if applied here, would cause interactions between micro-scale particles to be felt at unnecessarily long distances. Instead, our use of the LJ/SF potential allows an adjustable cut-off ($r_c \approx\ 1.5\,\sigma - 2\,\sigma$) while ensuring no discontinuity in potential and force at r_c. This makes it so particles in the model interact with each other smoothly near the cut-off distance if the LJ potential has a significant discontinuity at the cut-off distance, this can cause the simulation to become numerically unstable.

The standard LJ potential function is

$$U_{\mathrm{LJ}}(r) = \Phi(r_{\mathrm{c}} - r)\, 4\varepsilon \left[\left(\frac{\sigma}{r}\right)^{12} - \left(\frac{\sigma}{r}\right)^{6}\right] \tag{4.1}$$

where σ is the size of the particle, and ε is the attractive energy well depth, r_{c} is the cutoff distance, r is the distance between the particles, U_{LJ} is the LJ potential energy, and Φ is the Heaviside step function that can turn off the LJ potential function when r is larger than r_{c}.

In contrast, the LJ/SF potential function is

$$U_{LJ/SF}(r) = U_{\mathrm{LJ}}(r) + (r - r_c)\, F_{\mathrm{c}} - U_{\mathrm{c}}\ , \tag{4.2}$$

where
$$F_{\mathrm{c}} = \frac{24}{r_{\mathrm{c}}}\varepsilon \left[2\left(\frac{\sigma}{r_c}\right)^{12} - \left(\frac{\sigma}{r_c}\right)^{6}\right], \tag{4.3}$$

and
$$U_{\mathrm{c}} = 4\varepsilon \left[\left(\frac{\sigma}{r_c}\right)^{12} - \left(\frac{\sigma}{r_c}\right)^{6}\right]. \tag{4.4}$$

Particles of different size and type (i.e. active material or carbon domain) were assigned different LJ/SF parameters. Standard (Lorentz-Berthelot) combining rules are used for cross interactions [56] where i and j represent particle identities.

$$\sigma_{ij} = \frac{\sigma_{ii}+\sigma_{jj}}{2} \ , \ \varepsilon_{ij} = \sqrt{\varepsilon_{ii}\varepsilon_{jj}} \ , r_{c,ij} = \frac{r_{c,ii}+r_{c,jj}}{2} \tag{4.5}$$

The parameters used for DPP1 model are shown in Table 4.2, and they are based on empirical adjustment, similar to how the model was employed previously [25]. The active material diameter ($d_{a,\mathrm{exp}}$) varied according to the values given in Table 4.2. 5553 particles were used in DPP1 model: 53 of the particles were marked as active material, while the rest of the particles were carbon domain particles. The temperature of the model was controlled at 300 K.

Since the LJ/SF potential is a soft potential, there is a direct and unchanging relationship between σ and the experimental particle diameters. For instance, the diameter of carbon can be arbitrarily chosen to make simulated properties match their experimental values.

The simulation procedure is as follows, as illustrated in Figure 4.6. During a given simulation, the time increment or time step is taken to be Δt =1μs.

1. Randomly assign particles locations within a cubic box of length L=900 μm, which assuring that none of the particles are overlapped. The relatively large size of the box makes the non-overlapping easy to implement.
2. Move particles with initial velocities that correspond to the temperature. The simulation is run for $2 \cdot 10^4$ time steps.
3. Compress the cubic box equally in x, y, z directions until L=30.278 μm. Since the active material was designed not to overlap with each other in the model, this length allows us to match the volume fraction of active material in the calendered cathode. The simulation is run for 10^6 time steps.

Table 4.2. Parameters used for DPP1 model

Parameters	σ_a (μm)	σ_c (μm)	ε_a/k_B (K)	ε_c/k_B (K)	$r_{c,\mathrm{a}}$ (μm)	$r_{c,\mathrm{c}}$ (μm)
Values	$d_{a,\mathrm{exp}}$	1.1	1500 $d_{a,\mathrm{exp}}$	25	$\sigma_a \cdot 2^{\frac{1}{6}} + 2$	2 σ_c

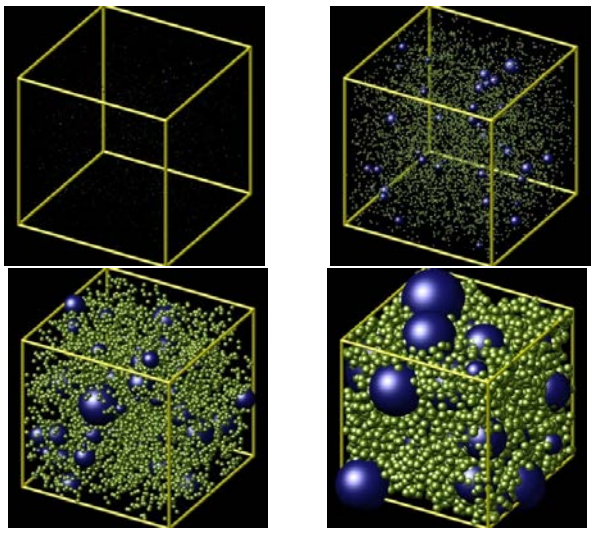

Figure 4.6. DPP1 model process simulating from the beginning to the final stable configuration. Box sizes are decreasing from left to right (particle sizes are constant). The final box size is 30.278 μm.

4. Run the main simulation for $2 \cdot 10^5$ time steps. An equilibrium final configuration is used as the electrode structure for subsequent analysis.

5. Output a dump file that stores the coordinate of each particle.

The simulated electrode structure was reconstructed as follows. The output file from LAMMPS is read by a C++ program to store the coordinate of each particle. The program then creates a 3D grid of cubic voxels (0.5 μm on each voxel edge), each of which has a specific coordinate. The total grid size is the same as the box used during the particle simulation. The program then assigns domain identities (active material, carbon domains, macro-pores) to each

voxel sequentially. After the grid is constructed and assigned domains, it is used to measure structural properties and output 2D slice images of the simulated cathode structure.

The following rules used in the assigning process. Active material domains are the first assigned. If the distance between a voxel and the center of an active material particle is less than the radius of that active material particle, the voxel is assigned active material. Next, carbon domains are assigned in the same fashion. A voxel can only be assigned as carbon if it was not previously assigned as active material. Finally, the leftover voxels are then assigned as macro-pores. This algorithm imitates the observation of the SEM image that carbon domains are softer than active material and surround the active material in irregular shapes.

In applying the above steps, the nearest-image method is applied to assign domains to each voxel in the periodic boundary box. This means one side of the grid is connected to the other size of the grid. For example, the arrows in Figure 4.7 point to voxels on opposite sides of the simulation box that are actually part of the same active material particle. The details for this method can be found in Ref. [57].

Figure 4.7. 30 μm × 30 μm slice from a DPP1 model configuration at 30% porosity. Blue represents active material domains, olive green represents carbon domains, white represents macro-pores. The arrows indicate voxels on opposite sides of the simulation box that are part of the same active material particle.

4.6 DPP2 model

4.6.1 Introduction

As described above, the DPP2 model was designed to simulate the slurry-coating, drying, and calendering processes. This means that the design goal for the DPP2 model is to be capable of performing well in both liquid and solid states as well as the transition from liquid to solid. In order to approach this goal the following four ideas are important.

The first idea was to keep most of the setup of the DPP2 model the same as the DPP1 model. For instance, The LJ/SF was kept in DPP2 because it is capable of simulating particles' interactions in the solid state by locking particles together through attractive interactions. In addition, one type of carbon domain particle and multiple discrete sizes of active material particle were kept in DPP2.

The second idea was to augment the potentials of particles with granular-type force field. All the particles have the same functional form composed of a linear combination of the LJ/SF potential and a granular-type potential. In this overall function, if the granular-type potential is dominant and controls behavior then the material acts more like a liquid. On the other hand if the LJ/SF potential is dominant and controls behavior then the material acts more like a solid.

The third idea for the DPP2 model was that the drying transition happens by changing some of the parameters in the two types of potentials. Specifically for the carbon particles there is one potential (force field) for liquid and another for solid. During the drying process the solvent evaporates and the binder starts to adhere active material particles with carbon black. The carbon solid potential is designed to be more attractive than the liquid potential. This attraction makes particles in the solid less likely to move, so the solid is stiffer than the liquid. Moreover, the solid potential makes the size of simulated solid relatively smaller than the size of simulated

liquid made by the liquid potential. This is because the solvent occupies most the space in the liquid. On the other hand, for the active particle the potential does not change during drying.

The fourth idea was to develop an active-free model to build up expertise before running the DPP2 model. There are several parameters used in the DPP2 model so finding satisfactory parameters was a big challenge. Hence, the approach was to use this prototype model to simulate the cathode without active material particles first (active-free model) to find carbon-carbon interaction parameters. Then, active material particles are added into the simulation (active-composite model), assuming carbon-carbon interactions stay the same.

4.6.2 Granular-type potential (force-field) in DPP2

As described above, the DPP2 model was designed to have a similar LJ/SF solid potential as DPP1 model, but DPP2 also includes a granular-type potential (force-field) to better imitate the liquid behavior in the slurry-coating process. The idea for the liquid-imitation force field is based upon a Brownian motion force field [58] designed to simulate the random motion of particles suspended in a fluid resulting from their collisions with other particles in the liquid or gas. Because a Brownian-motion-type simulation generates liquid behavior using an implicit solvent there are no extra particles required to simulate the solvent in the DPP2 model.

The Hertzian granular force field, designed for polydisperse systems, is used in the DPP2 model. The Hertzian granular pairwise force field has two terms as shown in Eq. 4.6. The first is a normal force component $\mathbf{F}_n$, a repulsive contact force between two particles generated when two particles collide with each other. The second is a tangential force component $\mathbf{F}_t$, the contact force between two particles generated when two particles slide past each other, creating a torque on each of them that could change the rate of rotation.

$$\mathbf{F}_{\mathrm{hz}} = \mathbf{F}_n + \mathbf{F}_t \tag{4.6}$$

where
$$\mathbf{F}_n = \sqrt{\delta}\sqrt{\frac{d_1 d_2}{2(d_1+d_2)}}\ (K_n\,\delta\mathbf{n} - m_{\mathrm{eff}}\,\gamma_n\,\mathbf{v}_n)\ , \tag{4.7}$$

$$\mathbf{F}_t = -\sqrt{\delta}\sqrt{\frac{d_1 d_2}{2(d_1+d_2)}}\,(K_t\,\Delta\mathbf{s}_t - m_{\mathrm{eff}}\,\gamma_t\,\mathbf{v}_t)\ , \tag{4.8}$$

$$\delta = (d-r)\,\Phi(d-r)\ , \tag{4.9}$$

$$d = \left(\frac{d_1+d_2}{2}\right), \tag{4.10}$$

and
$$m_{\mathrm{eff}} = \frac{m_1\,m_2}{(m_1+m_2)}\,. \tag{4.11}$$

The many variables in these equations are discussed below. $\mathbf{F}_n$ is composed of two terms, the normal distance-dependent force and the normal damping force. The first term is similar to LJ/SF potential, which generates a repulsive force when two particles contact each other in the normal direction. The second term in Eq. 4.7 is used to imitate the liquid behavior (implicit solvent) by slowing down the speed that particles move toward and leave each other. When particles are approaching, the implicit solvent between the particles is squeezed, and generates an opposing force to slow down the approach of the particles. Likewise, when particles are leaving each other, the implicit solvent generates forces that slow down the movement of the particles.

$\mathbf{F}_t$ is composed of two terms, the frictional contact force and the tangential damping force. The first term generates torque from one particle to another when they rotate relative to the line connecting the centers of each particle. The second term in Eq. 4.8 is like the second term in Eq. 4.7, but it applies in the tangential direction.

In the above equations m_{eff} is the reduced or effective mass of two interacting particles, m_1 and m_2; d_1 and d_2 are the diameters of two interacting particles, r is the distance between centers of the two particles. Φ is the Heaviside step function that can turn off the granular

potential when the distance, r, between the two particles is larger than their combined, average diameter, *d*. $\mathbf{v}_n$ and $\mathbf{v}_t$ are the relative normal and tangential velocity of two interacting particles, respectively.

Δs_t is the elastic tangential displacement between two interacting particles, obtained by integrating tangential relative velocities during elastic deformation for the lifetime of the contact, and is truncated as necessary to satisfy the Coulomb criterion $|\mathbf{F}_t| \leq x_\mu |\mathbf{F}_n|$ [59], in which x_μ is the friction coefficient. The tangential force between 2 particles grows according to a tangential spring and dashpot model until $|\mathbf{F}_t| = x_\mu |\mathbf{F}_n|$ under this condition until the particles lose contact [60];

K_n and K_t are the elastic constants for the normal force and tangential force between two particles, respectively. K_n and K_t control the amount of normal repulsion (head-on collisions) and tangential repulsion force (torque) exerted when two particles are overlapped; γ_n and γ_t are the corresponding damping coefficients for dissipating part of the collision energy for normal and tangential motion, respectively. Notably, $K_n, K_t, \gamma_n, \gamma_t, x_\mu$ are the only parameters for the granular force field determined by the user.

When both the granular force field and LJ/SF potential are used in the simulation, choosing parameters to have reasonable liquid and solid behaviors is challenging. Hence, an idea to mitigate this difficulty is to plot and analyze a simplified function that includes the LJ/SF potential and the normal component of the Hertzian granular force field, to assist in predicting how particles will interact and provide a range of acceptable values for each parameter before running the full DPP2 model. Because this simplified function is intended to predict the attractive or repulsive interactions between particles only in a stationary, normal (non-tangential) direction, the $\mathbf{v}_n$ in the second term of $\mathbf{F}_n$, and $\mathbf{v}_t$ and $\Delta\mathbf{s}_t$ in the first and second terms of $\mathbf{F}_t$ are

excluded. In this analysis, the Hertzian granular force needed to be transformed into a potential energy function by integrating over the distance between particles. The resulting simplified granular potential U_{gran} is

$$U_{\text{gran}} = \frac{2}{5} K_n \mu m^3 \left[\left(\frac{d_1}{2}\right)^{-1} + \left(\frac{d_2}{2}\right)^{-1}\right]^{-0.5} \delta \ . \tag{4.12}$$

One can combine Eq. 4.2 and Eq. 4.12 to obtain a combined potential U (Eq. 4.13) between the particles in the system.

$$U = U_{gran} + U_{LJ/SF} \ , \tag{4.13}$$

The standard combining rules (Lorentz-Berthelot rules) are also used in DPP2 model for cross interactions.

Figure 4.8 a and b show the LJ/SF and granular potential functions, respectively. The granular potential was designed to only repel neighboring particles when they become overlapped. On the other hand, the LJ/SF potential has both attraction and repulsion between particle interactions. This is reasonable for solid state because the attractive force can lock active material together with carbon domains and yet show repulsion if overlaps between particles become too great, as shown in the SEM image (Figure 3.2). The simplified-potential curves

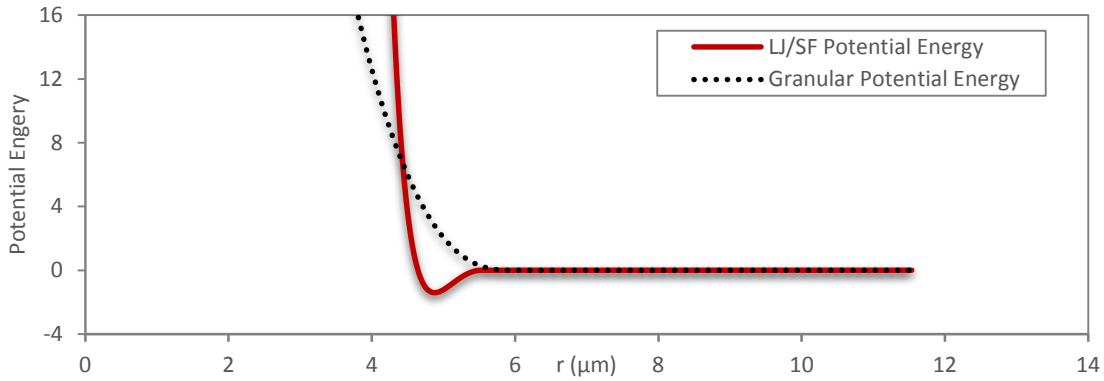

Figure 4.8 (a) granular potential function (b) LJ/SF potential function.

demonstrated above assisted in the analysis to determine optimal potential parameters, as discussed in Section 4.7 and 4.8.

4.7 Active-free model

4.7.1 Introduction

The active-free model was developed to help determine parameters for the DPP2 model. In designing this model we needed to answer two questions. The first question was how can the combination of the LJ/SF and granular potentials imitate the solid and the liquid behaviors separately? In other words, what parameters (and their values) can make the LJ/SF potential dominate and control the solid behavior while allowing the granular potential to dominate and control the liquid behavior? The second question was what parameter values will also make it so that the model can quantitatively reproduce liquid and solid properties such as slurry viscosity and film elasticity? These questions are answered in the following section.

4.7.2 Control of the liquid and solid behaviors

The granular potential is quite sensitive to the value of diameter *d*. Holding all other parameters constant, the relative strength of the LJ/SF and granular parts of the potential can be controlled with *d*. Figure 4.9 shows the combination of LJ/SF and granular potentials in the simplified function of the active-free model where different curves were computed using different granular diameters of carbon domain particles. When the diameter of the carbon domain particles is large interacting particles only feel repulsion. However, as the diameter of the carbon

domain particles decreases the potential becomes less repulsive until it develops an attractive well as two particles approach close to each.

In this work, two different carbon diameters were used during simulation. By switching the size of the carbon domain particles from a large one to a small one, the particle behavior can change from liquid to solid. The physical justification for using two different size of carbon domain particles is as follows. The carbon domain particles are composed of carbon black, binder, nano-pores, and solvent in the liquid state, while the carbon domain particles are composed of carbon black, nano-pores, and binder in the solid state. Thus, changing the size of the carbon domain particles during the simulation describes the fact that they shrink during drying process when the solvent evaporates from the slurry.

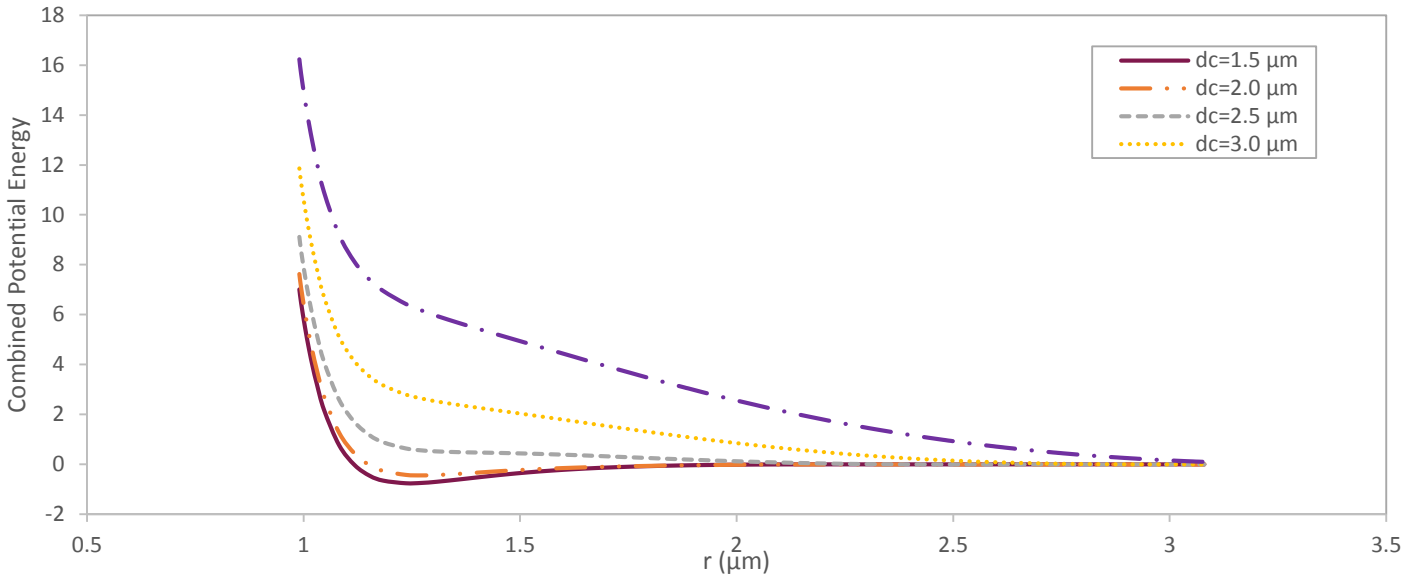

Figure 4.9: The combined potential in the simplified function diagram. Different colors represents different granular diameter of carbon domain particles, as showed in the right-top corner of the diagram. The LJ/SF part of the potential is held constant.

4.7.3 Determination of $d_{c,l}$ and $d_{c,s}$ for active-free model

To determine the granular force diameters of carbon domain particles for liquid ($d_{c,l}$) and solid ($d_{c,s}$), comparisons to experiment were made. Specifically, liquid viscosity, solid elasticity, and the shrink ratio (the ratio of the thickness of the original slurry to the final dried cathode) are the three main properties to be considered. First, the simulated viscosity can tell if the model imitates the liquid behavior well by using a reasonable value of $d_{c,l}$. Secondly, the elasticity can tell if the model imitates the solid behavior well by using a reasonable value of $d_{c,s}$. Finally, the shrink ratio can tell if the model imitates a reasonable drying process from liquid to solid.

Figure 4.10 shows the simulated viscosity of a slurry in the active-free model at different diameters of carbon domain particles d_c. One can find that the viscosity does not change significantly when d_c is larger than 2.6 μm. In addition, Figure 4.9 also shows the granular potential dominates the particles' interactions when d_c is larger than 3.0 μm. Therefore, it's estimated that the appropriate choice for $d_{c,l}$ is larger than 3.0 μm.

Since there is a range of acceptable values for $d_{c,l}$, we can determine $d_{c,s}$ first and then choose $d_{c,l}$ in the range to give the model the right shrink ratio. From Figure 4.9, we know a good value for $d_{c,s}$ is below 1.5 μm because the LJ/SF potential dominates. In addition, Figure 4.11 shows that the elasticity increases as d_c decreases. Here we choose 1.4 μm for $d_{c,s}$ because it generates the elasticity closest to the experimental value (9.03 MPa). Later, the elasticity can be further adjusted to better match the experimental value through adjusting another parameter such as ε_c. Here we don't use $d_{c,s}$ below 1.4 μm because this low of a value of $d_{c,s}$ makes the potential stiff, requiring the use of a smaller time step and reducing computational efficiency. Once the value for $d_{c,s}$ was chosen, $d_{c,l}$ was set to 3.3 μm to provide the right shrink ratio.

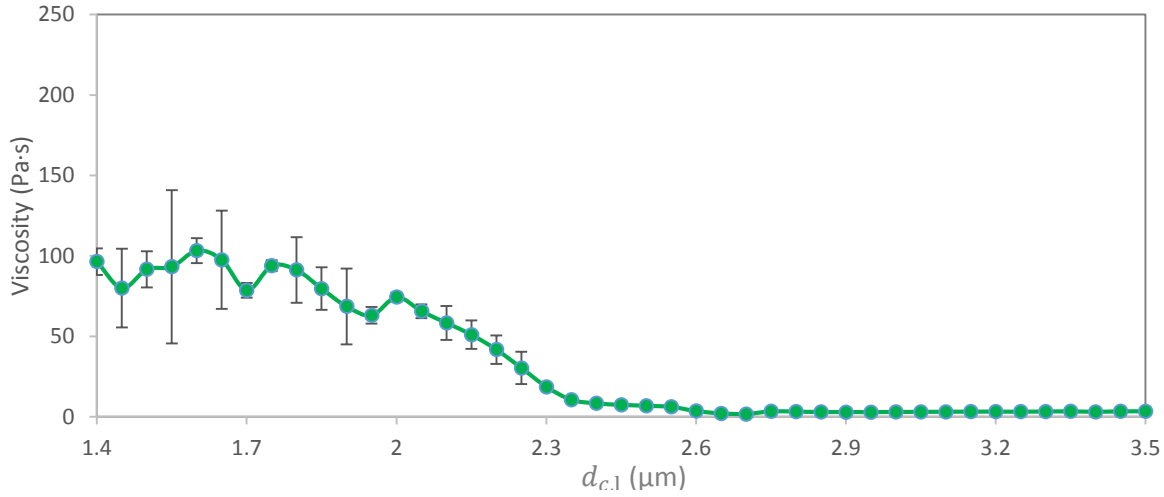

Figure 4.10. Simulated viscosity of the slurry in active-free model for different values of $d_{c,l}$. The line connecting points is a guide to the eye. Bars indicate 95% confidence intervals.

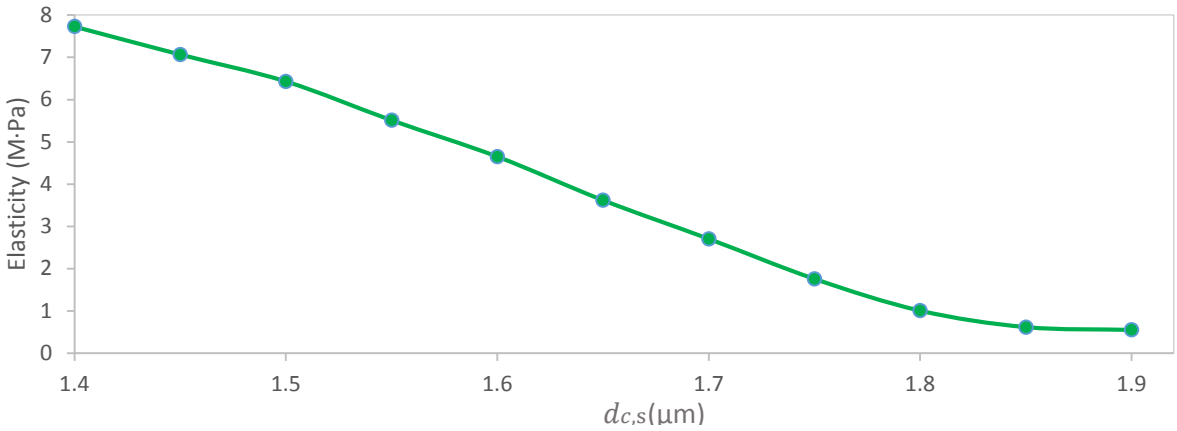

Figure 4.11. Simulated elasticity of the solid in the active-free model for different values of $d_{c,s}$. Line connecting points is a guide to the eye.

Table 4.3. Parameters used for active-free model

parameters	values
σ_c (μm)	1.1
r_c (μm)	2 σ_c
$\varepsilon_{c,\mathrm{l}}$ ($\frac{pg \cdot \mu m^2}{\mu s^2}$)	200
$\varepsilon_{c,\mathrm{s}}$ ($\frac{pg \cdot \mu m^2}{\mu s^2}$)	500
$\rho_{c,\mathrm{l}}$ ($\frac{gm}{cm^3}$)	0.6968
$\rho_{c,\mathrm{s}}$ ($\frac{gm}{cm^3}$)	0.78
$d_{c,\mathrm{l}}$ (μm)	3.3
$d_{c,\mathrm{s}}$(μm)	1.4
K_n (MPa)	500
K_t (MPa)	680
γ_n ($\frac{1}{\mu s \cdot \mu m}$)	0
γ_t ($\frac{1}{\mu s \cdot \mu m}$)	0
$x_{\mu,\mathrm{l}}$	0.001
$x_{\mu,\mathrm{s}}$	1

4.7.4 Determination of other model parameters for active-free model

$d_{c,\mathrm{l}}$, $d_{c,\mathrm{s}}$ and other model parameters were determined iteratively because to some degree they all have effects on particle interactions and thus simulated properties. For instance, $d_{c,\mathrm{l}}$ and $d_{c,\mathrm{s}}$ control the relative magnitudes of the granular and LJ/SF potentials. Other model parameters likewise control the shape of the combined potential. Nevertheless, we attempted to identify the parameters to which properties were most sensitive and then used other parameters to refine the results as described below.

The parameters used for the active-free model are shown in Table 4.3. σ_c and r_c are the σ value and cut-off distance for interactions between carbon domain particles, and are the same as those in the DPP1 model. $\varepsilon_{c,\mathrm{l}}$ and $\varepsilon_{c,s}$ are the ϵ values for liquid and solid carbon domain particles, respectively. Originally $\varepsilon_{c,\mathrm{l}}$ and $\varepsilon_{c,s}$ were the same, but the low value of $\varepsilon_{c,s}$ gave the dried cathode too small of an elasticity compared to experimental values. This was corrected by using a higher value for $\varepsilon_{c,s}$ because ε is related to the modulus of elasticity. This describes the fact that the carbon domain particles interactions should be strong after the solvent evaporates. $\rho_{c,\mathrm{l}}$ and $\rho_{c,s}$ were particle densities for liquid and solid carbon domains. The values for the particle densities were adjusted until the mass density (calculated by dividing the total mass of the carbon domain particles by the box volume) of simulated liquid and solid matched to the experimental values of the uncalendered active-free slurry and cathode film.

Granular parameters K_n, K_t, γ_n, γ_t, and x_μ were adjusted until the simulated viscosity matched or was close to experimental values. γ_n and γ_t were initially set to 0 based on Ref.[59, 61]. Then we tried two magnitudes of different γ_n and γ_t, but we found that they did not show a significant effect on the viscosity. Hence, γ_n and γ_t were set to 0. On the other hand, K_n and K_t were set to the ratio $K_n = 0.693\ K_t$ based on the Ref. [62]. From the viscosity simulation, we found that decreasing K_n can decrease the viscosity of the liquid. K_n was set to 500 MPa so that the resulting viscosity is close to the experimental value.

x_μ, as mentioned above, is the friction factor that controls the upper limit of the tangential force. One can image that the tangential force between particles in liquid is relatively low but much stronger in the solid. Hence, it is reasonable to use high x_μ for solid and low x_μ for liquid. Table 4.4 shows the viscosity at different values of x_μ for liquid and solid. As x_μ increases, the viscosity increases. For the liquid x_μ is set to 0.001 so that the liquid viscosity is lowest and close

to experimental viscosity. On the other hand, the solid viscosity in reality is effectively infinite, but this value cannot be computed in simulation. Hence, we set the solid x_μ to 1 (the maximum value recommended by LAMMPS documentation) to have sufficiently large solid viscosity.

Table 4.4. Simulated viscosity of the slurry in active-free model at different x_μ for liquid and solid.

x_μ	Liquid Viscosity (Pa·s)	Solid Viscosity (Pa·s)
0.001	3.3	30
0.01	4.4	30
0.1	7.0	91
1	11.6	116

4.7.5 Simulation of active-free model

The active-free model was started by generating an equilibrium structure representing a well-mixed slurry of the desired composition. During drying, the solvent evaporates from the slurry and the simulated box shrinks until the ratio of the thicknesses of the original slurry and dried cathode is correct. Finally, a stable solid structure is formed. The method that was used to segment the simulated microstructure into a 3D grid done for the DPP1 model is also used here (see Section 4.5).

There are few simulation details in the active-free model that are different from DPP1 model, described as follows. The whole simulation of active-free model was held constant at 1 bar pressure since electrode manufacturing takes place in ambient conditions. The simulation time for the active-free model was 7.1×10^7 time steps, each of time increment Δt =0.001μs, to reach a stable final configuration which was used as the electrode structure. Here, 11000 carbon domain particles were used instead of the 5500 carbon domain particles used in DPP1, in order to increase the size of the final structure to better match the thickness of a real cathode. The

length in the z direction was set longer than the length in the x and y directions to better simulate the drying process, which causes shrinkage in the z direction. The simulation of the solid state used the final structure from the liquid state simulation as the starting configuration, but with the diameter of carbon domain particles changed from $d_{c,\mathrm{l}}$ to $d_{c,s}$.

The simulation steps are as follows, as illustrated in Figure 4.12.

1. Assign particle locations randomly within an elongated box of length L=900 μm in x and y direction, and L=3600 μm in z direction. The relatively large box size ensured that particles did not overlap one another.
2. Move particles with initial velocities that correspond to the temperature, 300 K.
3. Run the simulation under NPT control with the pressure set to 1 bar. The elongated box starts adjusting its size to reach the set up pressure.
4. Generate an equilibrium structure representing the well-mixed slurry, which is shown in the first image of Figure 4.12.
5. Take this structure to measure the viscosity by NEMD method.
6. Change the diameter of carbon domain particles from $d_{c,\mathrm{l}}$ to $d_{c,s}$. The elongated box starts shrinking because the granular potential energy instantaneously diminishes and the LJ/SF potential dominates particles' interactions. This process imitates the drying of the slurry when the solvent evaporates. The drying process is shown in Figure 4.12.
7. Generate an equilibrium structure representing the dry active-free film, which is shown in the last image of Figure 4.12.
8. Use this structure to determine the elasticity.
9. Output a dump file that stores the coordinate of each particle.

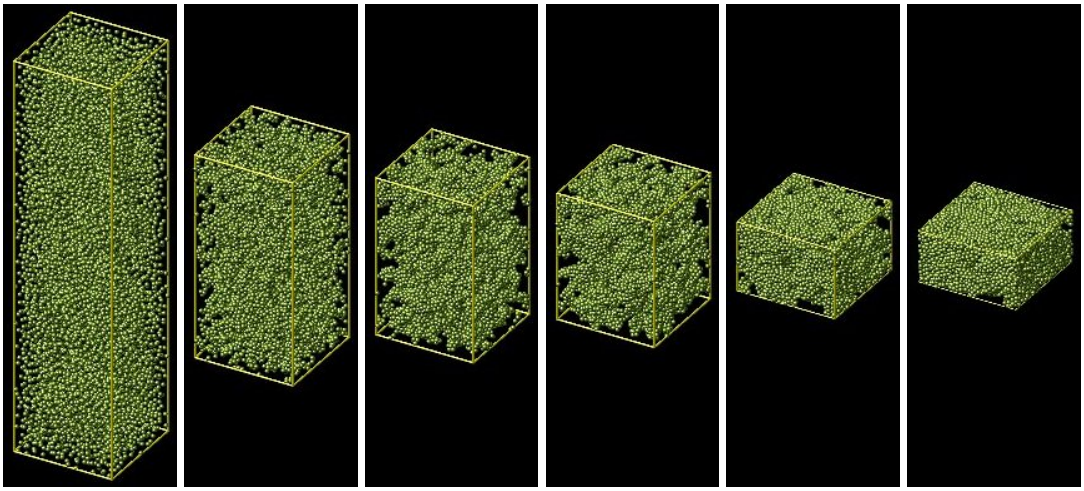

Figure 4.12. Drying on shrink process of the active-free model.

In summary, the active-free model was developed to help set values for some of the parameters used in the DPP2 model. After the active-free model successfully simulated the liquid, solid, and drying processes, work began on the active-composite model (DPP2 model). The active-composite model includes active material particles, and it was designed to generate reasonable liquid, solid, and drying behaviors through adjusting an additional few parameters. The details of active-composite model are discussed in next section. A discussion of how well the active-free model did in matching experiment is in Section 4.10.

4.8 Active-composite model

4.8.1 Introduction

The active-composite model is made by adding active material into the active-free model. In designing this model we needed to answer two questions. First, how many active material and

carbon domain particles are needed in a simulation? The basis for this question is that the ratio of active material and carbon domain particles can cause different solid and liquid behavior, which can cause the simulation to deviate from experiment. Second, how should we choose the force field parameters for the active-composite model? The active-free model helps determine the LJ/SF parameters of the carbon domain particles and most of the granular parameters for all particles in the system (K_{n}, $\mathrm{K_t}$, γ_{n}, γ_{t}, x_{μ}). The remaining parameters to be determined for the active-composite model are Lennard-Jones (σ_a, ε_a, $r_{c,\mathrm{a}}$) and granular size and mass parameters (d_a, m_a), which affect the particle behavior in liquid and solid states. This is complicated by the fact that multiple sizes of active material particles are used.

4.8.2 Determination of the number of active material and carbon domain particles

Since the active-composite model simulates the real process from a liquid to solid, it is necessary to use the experimental mass ratio of active material to carbon domain particles in the model. The number of active material particles was fixed to 106 (including all sizes), double the amount used in the DPP1 model. This was done because we aimed to increase the size of the final structure to better match the thickness of a real cathode, as described in the active-free model. The crystalline particle density of NCM active material is constant, so the total mass and volume of the active material is fixed. The particle density of carbon domain solid (carbon, binder, and nano-pores) is fixed from the active-free model, so the total mass of carbon domain particles only depends on the number of carbon domain particles used in the active-composite model. Hence, the simulated mass ratio was adjusted to match to the experimental value by

setting the number of carbon domain particles to 14496. This number is much higher than in the DPP1 model corresponding to a smaller carbon particle size.

4.8.3 Active material parameters for the model

In order to find the Lennard-Jones and granular size and mass parameters for the active material, a baseline case and sensitivity analysis were used. We picked a baseline for these parameters and analyzed their effect on the liquid and solid behavior by decreasing or increasing the parameter values. This can help us determine best parameters for the active-composite model to achieve a reasonably accurate liquid and solid behavior, including the final structure. The baseline and final values for each parameter used in the active-composite model are shown in Table 4.5.

A key concept in our model is to use simplified rules that relate one parameter to another. As shown in Table 4.4, there are 4 active material parameters and 8 particle sizes used in the model. This means there can be 32 parameters that need to be determined if the simplified rules are not used. The simplified rules are as follows: $r_{c,\mathrm{a}}$ is set as a function of σ_a; σ_a is set as a function of $d_{a,\mathrm{exp}}$; ε_a is set as a function of $d_{a,\mathrm{exp}}$. The next several pages discuss how these rules were developed.

In this work, the simplified function was used to assist in understanding and predicting the liquid and solid behavior during the sensitivity analysis. For example, changing σ_a and ε_a can change the curve of the LJ/SF and granular potentials. If the granular potential energy is not high enough, LJ/SF attractive interactions can cause the viscosity of a liquid to increase. On the other hand, if the LJ/SF potential energy is too low, then there is not enough attraction to lock active material particles with carbon domain particles. This can cause low elasticity of the solid. More

details about how active material parameters for the combined potential function were determined are discussed below.

Figure 4.13 shows the final simplified function demonstrated for three experimental particle diameters: $d_{a,\text{exp}}$ = 2, 10, and 15 µm. These three values were chosen as representative of interactions between relatively small, medium, and large particle sizes. One can observe the changes in this function in going from liquid to solid. Note that in order to illustrate the effect of parameter changes on a particle-to-particle potential energy, we picked one intermediate size of $d_{a,\text{exp}}$ ($d_{a,\text{exp}} = 9.952$ µm) for use in Figures 4.14 and 4.15 below.

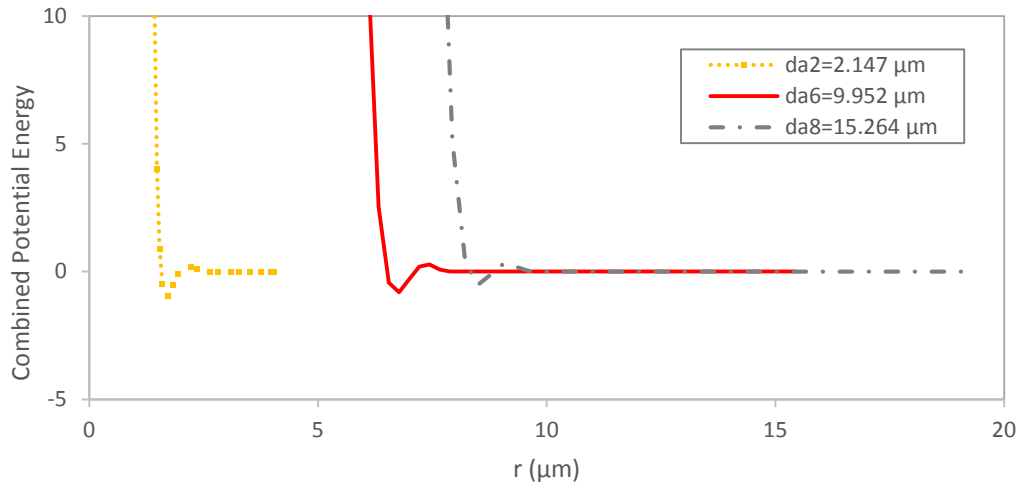

(a)

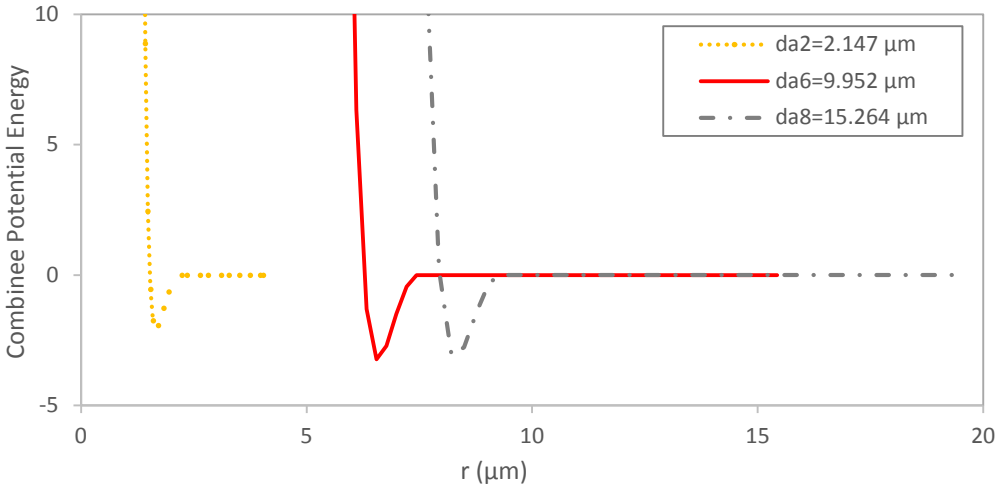

(b)

Figure 4.13. Combined potential function plot with different size of active material for (a) liquid state (b) solid state.

Table 4.5 Active material parameters for the model.

Baseline	Final
$\sigma_a = d_{a,\text{exp}}$	$\sigma_a = 0.84\ d_{a,\text{exp}}$
$\varepsilon_a = 500\left(\frac{d_{a,\text{exp}}}{\mu m}\right)^3\left(\frac{pg\ \mu m^2}{\mu s^2}\right)$	$\varepsilon_a = 800\left(\frac{d_{a,\text{exp}}}{\mu m}\right)^3\left(\frac{pg\ \mu m^2}{\mu s^2}\right)$
$d_a = r_{c,\text{a}} = \sigma_a$	$d_a = r_{c,\text{a}} = 1.27\ \sigma_a$

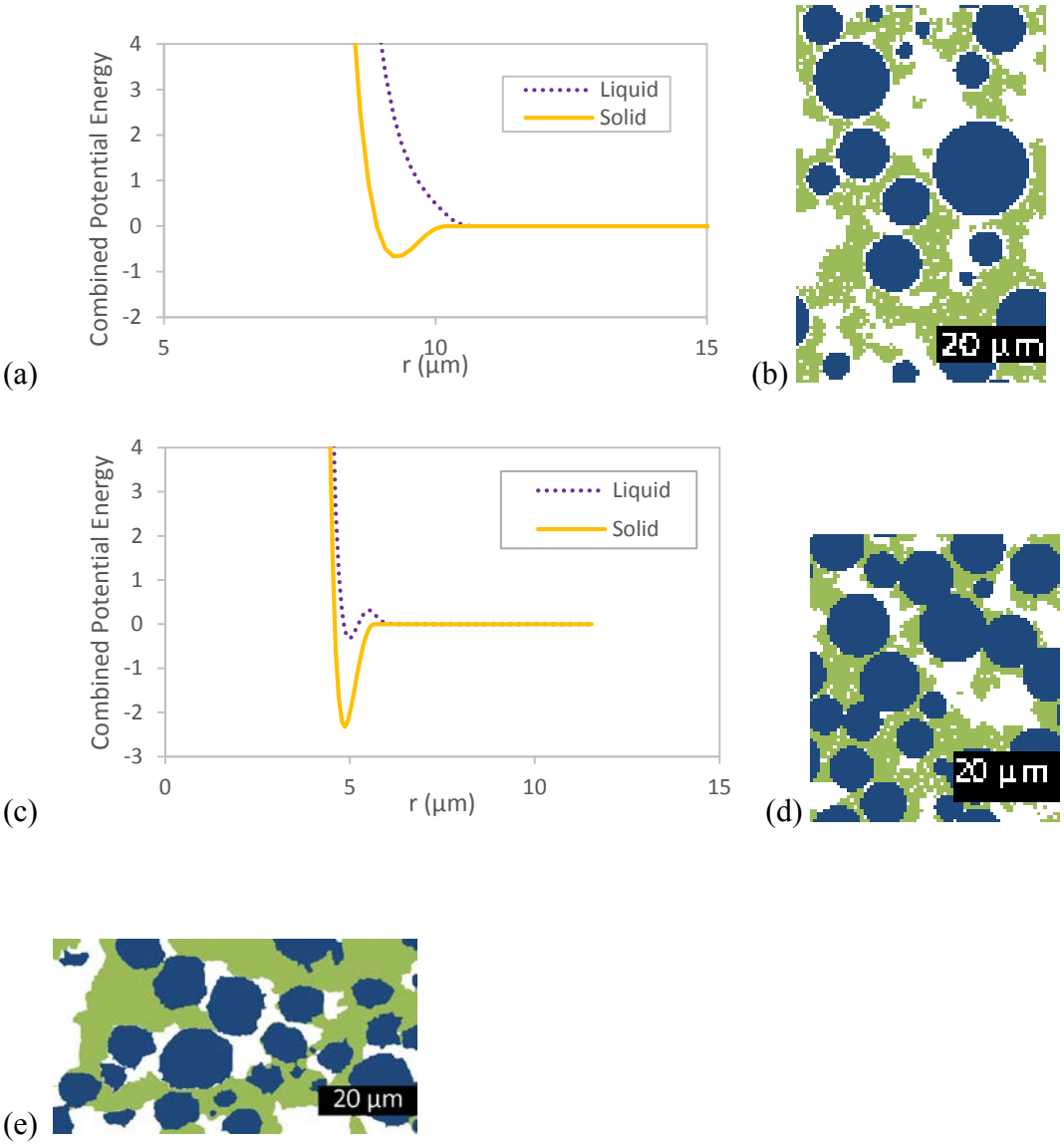

Figure 4.14. Potential function of the particle interactions between active material and carbon domain particles and the 2D cross section images of the simulated structure at (a)(b) $\sigma_a = 1.2\ d_{a,exp}$ (c)(d) $\sigma_a = 0.8\ d_{a,exp}$, and (e) the image of the uncalendered cathode.

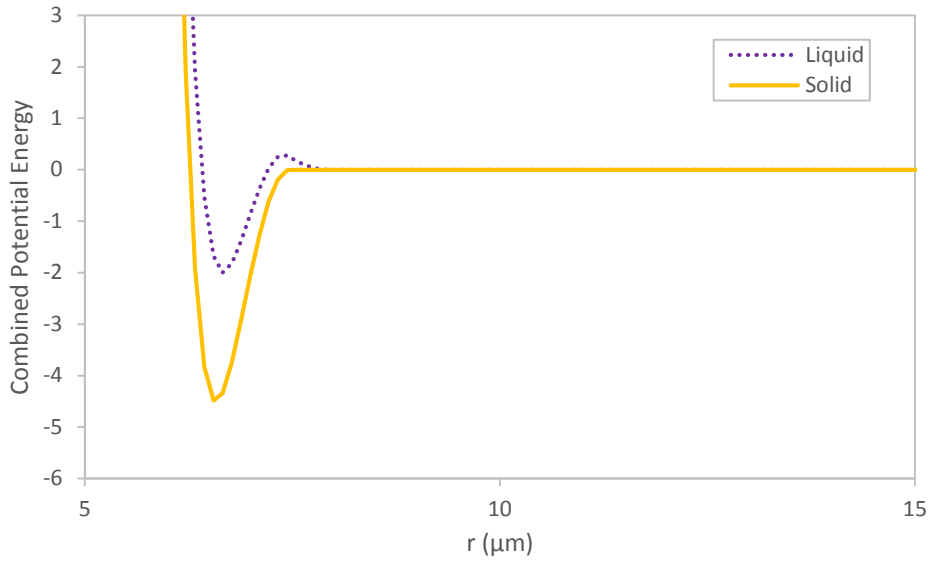

(a)

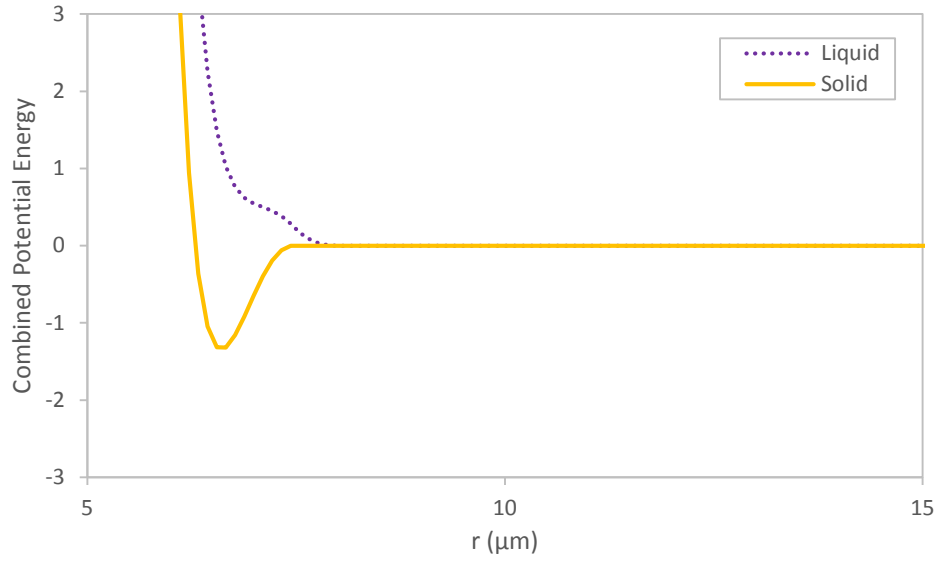

(b)

Figure 4.15. Potential function of the particle interactions between active material and carbon domain particles at (a) $\varepsilon_a = 1000\ (d_{a,exp})^3$ (b) $\varepsilon_a = 100\ (d_{a,exp})^3$.

4.8.4 Determination of $r_{c,\mathrm{a}}$, d_a, ρ_a

When we examined the effect of the LJ cut-off $r_{c,\mathrm{a}}$ on the liquid and solid behavior, we found that higher $r_{c,\mathrm{a}}$ caused more attraction between active material and carbon domain particles in both solid and liquid, while a lower $r_{c,\mathrm{a}}$ decreases attraction. Thus, $r_{c,\mathrm{a}}$ appears to

modify the attractive potential similar to ε_a. However, unlike ε_a, the parameter has little effect on the repulsion between particles at short range. For simplicity in the model $r_{c,\mathrm{a}}$ was always chosen to be equal to d_a. An additional benefit of this choice is that the computational cost is optimized when the LJ/SF and granular potentials have the same spatial cut-off.

σ_a and d_a are the respective LJ/SF and granular diameters used in the active-composite model instead of $d_{a,\mathrm{exp}}$, the experimental diameter of active material. This distinction is necessary because we use soft-sphere potentials instead of hard-sphere potentials, which means particles are allowed to overlap partially with other particles. In this condition, $d_{a,\mathrm{exp}}$ is an effective diameter of active material, but is not directly used in the potential functions to generate particle interactions. Hence, we chose a simple linear rule for the granular and LJ/SF diameters of the active material used in the active-composite model to have appropriate particle interactions (Table 4.5).

LAMMPS uses a particle density along with d_a to compute each particles mass. The experimental crystal density for our active material ($\mathrm{LiNi_{0.5}Co_{0.2}Mn_{0.3}O_2}$) is ρ_{ao}= 4.79 $\frac{\mathrm{gm}}{\mathrm{cm^3}}$ [48]. Because $d_a \neq d_{a,\mathrm{exp}}$ for the final model, the density ρ_a given for LAMMPS must be adjusted to generate the correct experimental particle mass:

$$\rho_a = \rho_{ao} \left(\frac{d_{a,\mathrm{exp}}}{d_a}\right)^3 \tag{4.10}$$

For example, the particle density ρ_a used in the DPP2 model is 4.48 $\frac{\mathrm{gm}}{\mathrm{cm^3}}$, which is 6% smaller than ρ_{ao}.

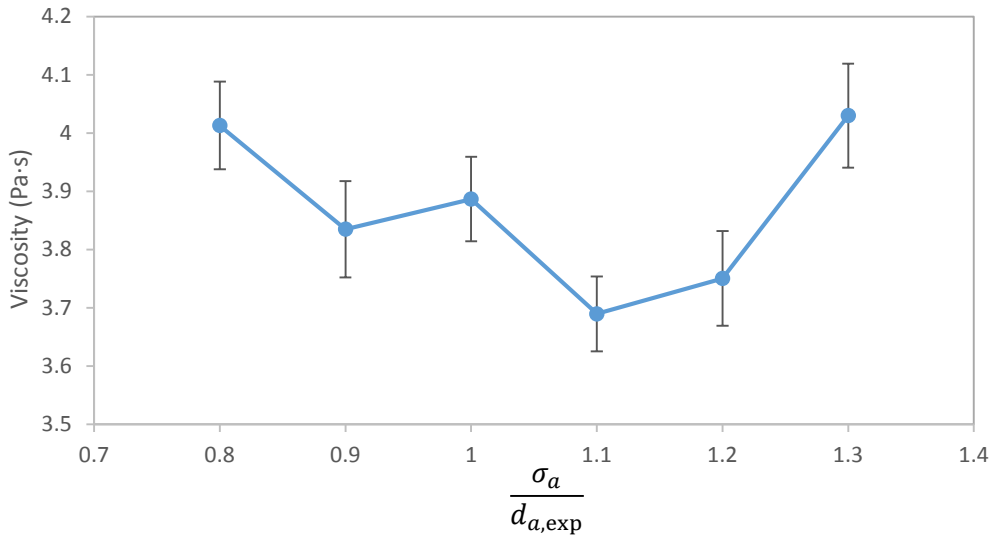

Figure 4.16. Viscosity plot at different σ_a. Line connecting points is a guide to the eye. Bars indicate 95% confidence intervals.

4.8.5 Determination of σ_a

To choose the ratio between LJ/SF parameter σ_a and $d_{a,\exp}$ (Table 4.5) for the active-composite model, we first examined the effect of σ_a on the liquid behavior. We used the baseline value for σ_a and then tested values higher or lower than this baseline value. We found that the viscosity of the liquid did not change significantly with σ_a, which is shown in Figure 4.16

Secondly, we examined the effect of σ_a on the solid behavior. Here we used the simplified function to assist in understanding and predicting the solid behavior. Figure 4.14 a and c shows the potential function of the particle interactions between active material and carbon domain particles at larger and smaller σ_a values, respectively. From Figure 4.14 a, where σ_a is larger, one can find that the depth of the potential function is shallow, which indicates the interactions between active material and carbon domain particles are less attractive. The 2D cross section image of the simulated structure shown in Figure 4.14 b depicts this weakly-attractive

behavior. Active material repels the carbon domain particles causing them to be surrounded by macro-pores. This phenomena causes the simulated structure not to match the experimental structure (Figure 4.14 e).

From Figure 4.14 c, where σ_a is smaller, one can find that the depth of the potential function is much deeper, which indicates the interactions between active material and carbon are more attractive. Figure 4.14 d shows strong interactions between the particles. The active material is now surrounded by the carbon domain particles and macro-pores. Here, the size of macro-pores are not large compared to the experimental structure. However, some of the active material particles are overlapped, which means that σ_a needs to be adjusted to a higher value than that shown in Figure 4.14 d. By iteratively adjusting the value of σ_a many times the best σ_a for the active-composite model was determined. The final σ_a value used in the model is shown in Table 4.5.

4.8.5 Determination of ε_a

Picking ε_a as a cubic function of $d_{a,\text{exp}}$ is partly empirical. We wanted to have stiff potentials with a small amount of attractive component, for all size of particles. Theoretically, it makes sense that ε_a would increase with particle size, because the attraction between particles is governed by van der Walle forces, which in turn depend on mass or volume of material in each particles.

After adjusting the value of σ_a we then attempted to find an optimal value of ε_a in the LJ/SF potential to further improve the agreement between the simulated and experimental structures for the liquid and solid states. We again used the baseline value for ε_a and tested values higher or lower than this baseline value. Figure 4.15 shows the interaction between active

material and carbon domain particles in liquid and solid at high and low ε_a. We found that higher ε_a caused the depth of the potential well to be shallow, which indicates that the magnitude of ε_a affects the liquid state behavior. The simulation results demonstrated that using larger ε_a increases the viscosity of the liquid, which is shown in Figure 4.17. Also, Figure 4.15 a and b shows how the solid particle interactions are strong enough for the active material to lock carbon domain particles into adjacent locations. Hence, a larger value of ε_a does not significantly affect the solid structure.

We also tested lower values of ε_a in the model. From Figure 4.18, we found that using a lower ε_a generates low elasticity. Thus, there is a tradeoff between elasticity and viscosity. Because of this limitation we decided to have the elasticity match to the experimental value at the cost of less accurate viscosity in the model. Table 4.5 shows the final ε_a values used in the model.

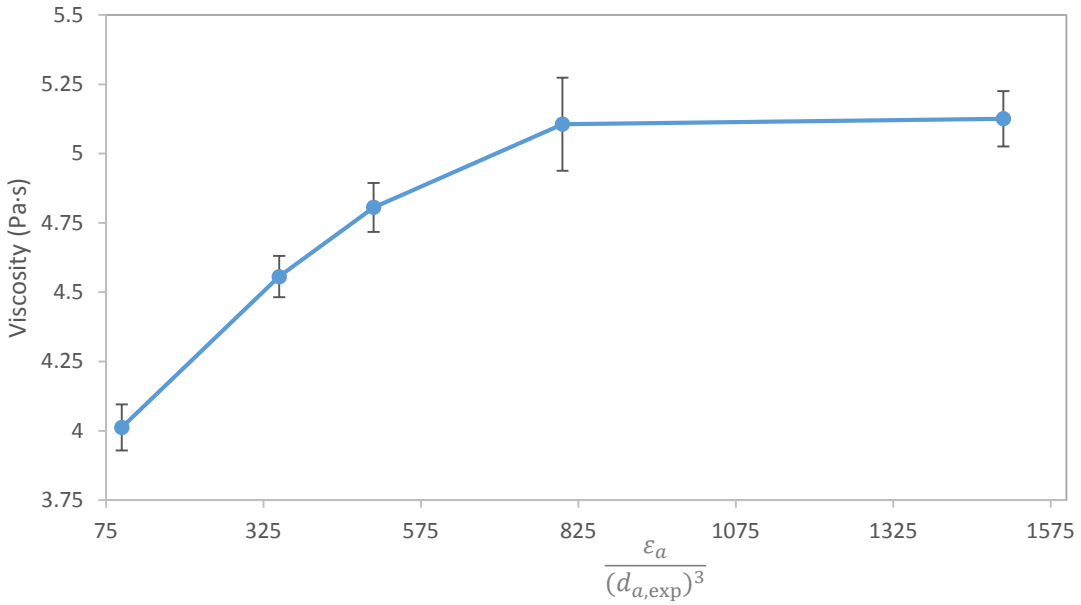

Figure 4.17. Viscosity plot at different ε_a . Line connecting points is a guide to the eye. Bars indicate 95% confidence intervals.

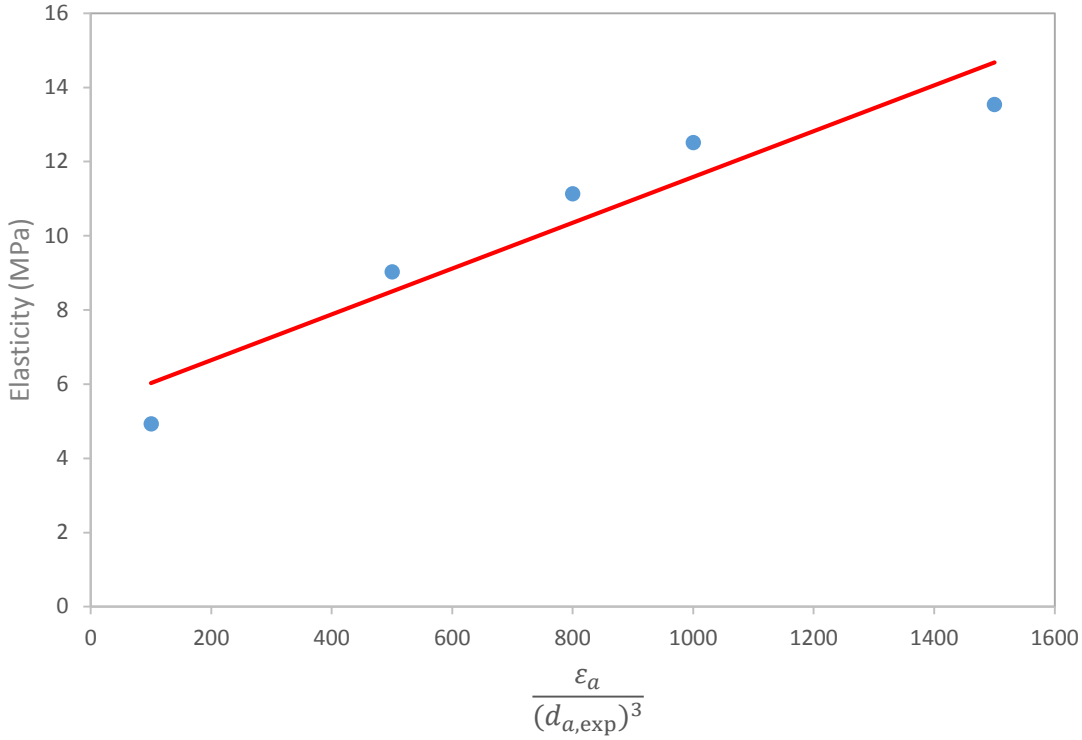

Figure 4.18. Elasticity plot at different ε_a. The experimental value for the simulated material is around 11 MPa. The solid line is a least squares regression line.

4.8.6 Simulation of active-composite model

Once the DPP2 model was parameterized, attention was turned to investigate the slurry coating and drying processes. The simulation setup for active-composite model was the same as it was for the active-free model (see Section 4.5). The same method used to reconstruct the simulated microstructure into a 3D grid done for the DPP1 model was used as well (see Section 4.5). The simulation processes for liquid and solid are shown in Figures 4.19. A discussion of how well the active-composite model did in matching experiment is in Section 4.10.

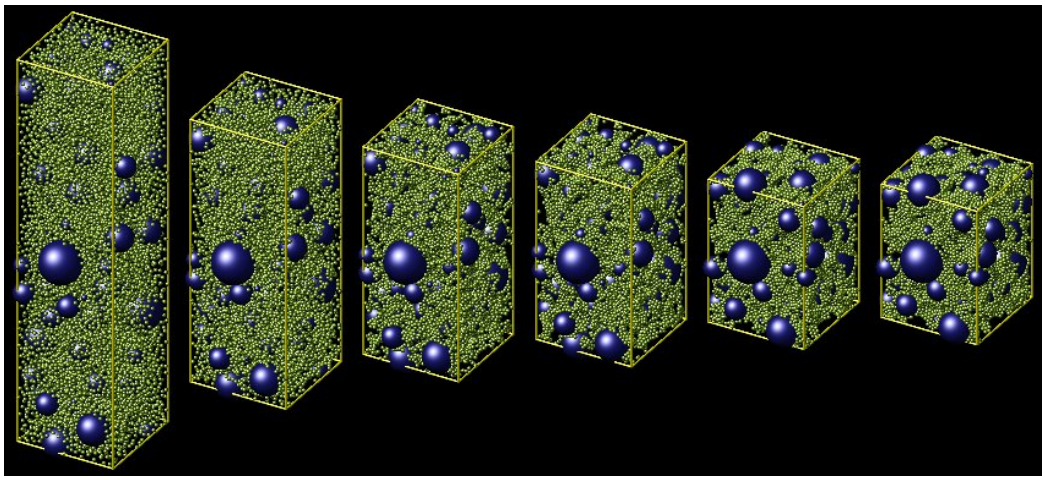

Figure 4.19. Drying or shrink process of the active-composite model.

(a)

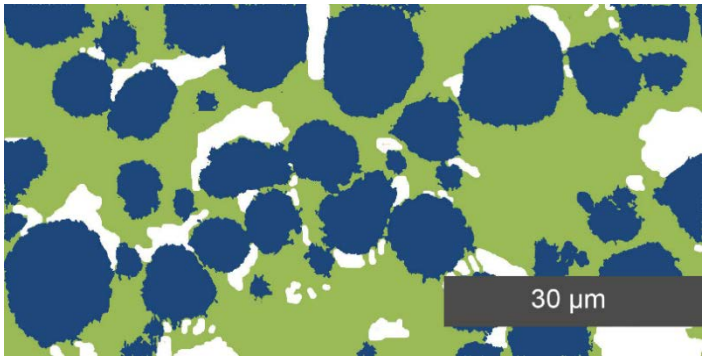

(b)

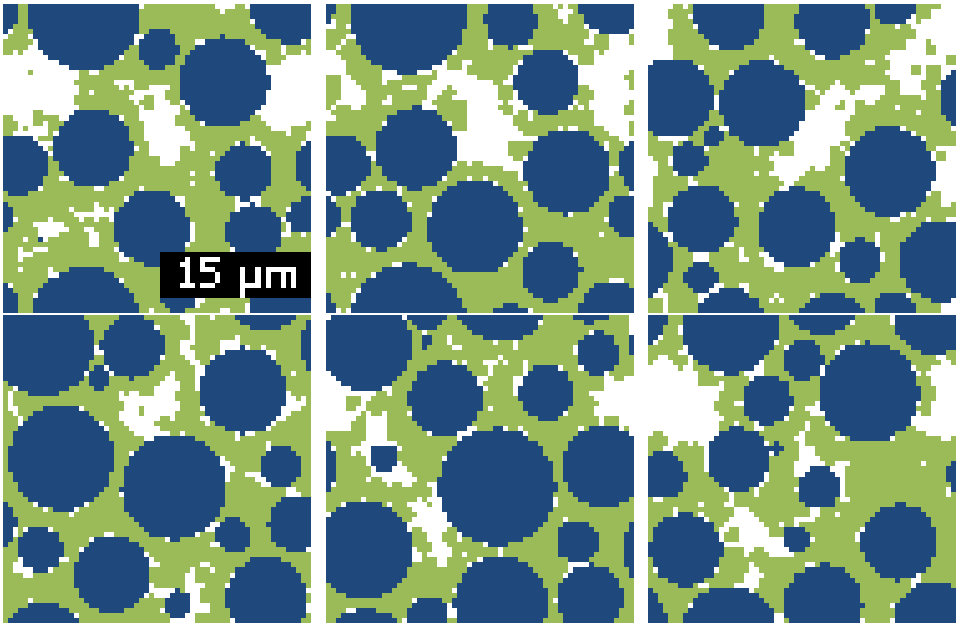

Figure 4.20. 2D cross section images of (a) experimental calendered cathode (b) simulated cathode of DPP1 model.

4.9. Comparisons of DPP1 model and calendered cathode electrode

For results if the DPP1 model, we only include a qualitative image comparison with a calendered cathode. Though additional microstructure properties were obtained, such as pairwise probabilities, they are not included here. This is for the sake of brevity and because the DPP1 model was used to help develop the DPP2 model, and is inferior to the DPP2 model. Figure 4.20 shows 2D images of calendered NCM cathode and the corresponding simulated microstructure of the DPP1 model. For the calendered cathode, most of macro-pores are surrounded by the active material particles. For the simulated microstructure, the DPP1 model did generate similar distribution of macro-pores like Figure 4.20 a. However, a smaller amount of macro-pores appear on the surface of active material. In addition, some of macro-pores are fractured instead remaining in solid shapes.

The arrangement of active material particles in Figure 4.20 a and b are similar, in which active material particles are generally separated from other active material. Nevertheless, the shape of active material in both images are slightly different. This is because a spherical shape was used in the DPP1 model to represent the active material particles, while active material particles used in the cathode were irregular shapes. The same issue recurs with the DPP2 model.

Table 4.6 Mass Density of DPP2 model and experiment $\left(\frac{gm}{cm^3}\right)$. 95% confidence intervals for simulations are also given.

Mass Density	Experiment	Simulation
Active-free liquid	1.03	1.03±0.00009
Active-free solid	0.70	0.70±0.015
Active-composite liquid	1.65	1.63±0.001
Active-composite solid	2.03	2.36±0.019

Table 4.7 Shrink ratio of DPP2 model and experiment. 95% confidence intervals for simulations are also given.

Shrink ratio	Experiment	Simulation
Active-free	8.03	7.98±0.17
Active-composite	3.26	2.96±0.03

4.10. Comparisons of DPP2 model and uncalendered cathode

To evaluate the robustness of the DPP2 model, structural and mechanical properties obtained from active-free and active-composite simulations were compared to uncalendered active-free film and uncalendered cathode, respectively. In addition, the experimental density and shrink ratio were used to validate that the DPP2 model has reasonable liquid and solid.

4.10.1 Mass density and shrink ratios

Experimental solid and liquid mass densities are basic properties that should be replicated by the DPP2 model. Mass density is used here to distinguish from other densities that are used in this work. Table 4.6 shows the mass density produced from multiple simulations using the two models as well as the experimental values. The experimental values were obtained through a one-time measurement on either a 20 cm^3 liquid sample or a 5 cm^2 film. The simulated active-free liquid and solid density are essentially equal to the experimental values. This is because the carbon domain particle liquid and solid density ($\rho_{c,l}$ and $\rho_{c,s}$) in the active-free model are adjustable to make the match. On the other hand, the active-composite liquid and solid densities are 1.21% below and 16.26% above the experimental values, respectively. This is because particle densities ($\rho_{c,l}$ and $\rho_{c,s}$, ρ_a) are fixed when the active-composite model is applied. So the real density of the active-composite model is determined solely from the physics of the

particle packing. Notably, the 95% confidence interval of the simulated liquid and solid densities of active-free and active-composite model are relatively small, which indicates that density is a highly reproducible property of the simulations.

There are two similar ways one can change the mass density of the simulated active-composite solid to match the experimental value. The first way is to adjust the LJ/SF particle size σ_a. For instance, increasing σ_a can cause more repulsions between active material particles and carbon domain particles, which makes the simulated box expand further to lower the mass density. However, as shown in section 4.8.5, using higher σ_a can cause active material particles to repel all particles that are approaching them including the carbon domain particles, causing the active material particles to be surrounded completely by macro-pores. The second way to increase the mass density is to adjust the granular active material particle size d_a(Eqn. 4.10). When a lower d_a is adopted the total volume of the system decreases, which increases the mass density. Also, changing solid or liquid density will affect the shrink ratio at the same time (trade-off).

Table 4.7 shows the shrink ratio of liquid to solid of active-free and active-composite models. The shrink ratio of active-free model is 0.62% above the experimental value. As described before, choosing an appropriate size of carbon domain for liquid and solid in active-free model can generate the right shrink ratio to match the experimental value. On the other hand, the shrink ratio of the active-composite model is 9.2% below the experimental value. Again, the error is the active-composite model is somewhat higher than in the active-free model. In the former case, the shrink ratio is not controllable independently because the sizes of carbon domain particles and active material particles are fixed.

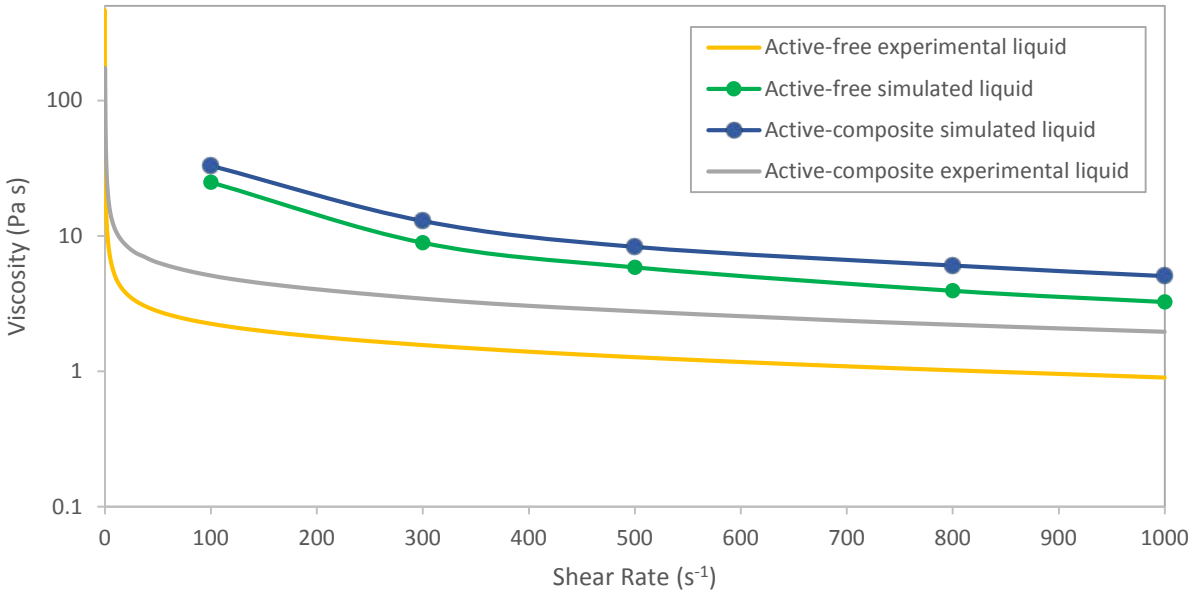

Figure 4.21 Viscosity vs. shear rate for simulations and experiment. Lines for simulations are a guide to the eye.

Table 4.8 Experimental and simulated elasticity (units MPa). 95% confidence intervals for simulations are also given.

Film	Exp	Sim
Active-free solid	9.03±0.86	10.1±1.3
Active-composite solid	11.32±0.72	11.7±1.2

4.10.2 Viscosity and elasticity

Figure 4.21 shows the liquid viscosity of the experiment and the two models at different shear rates. The viscosity experimental values were obtained by a one-time measurement. The simulated viscosity of both models are obtained through a one-time simulation because the viscosity simulation is considered reliable. This is shown in section 4.8.5 for the sensitivity analysis of ε_a with viscosity, in which the 95% confidence interval of the simulated viscosity values are around 0.1 to 0.3 Pa·s.

When the shear rate decreases, the viscosity of the two experimental slurries gradually increases, and rapidly goes to higher values as shear rate drops below 30 s^{-1}. In addition, adding active material particles in the active-free slurry further increases the value of the viscosity. This shear-thinning behavior is characteristic of slurries and is to be expected. The viscosity of the two simulated slurries shows the same pattern—the simulated active-composite slurry has a higher viscosity than the simulated active-free slurry and the simulations exhibit shear thinning. However, the viscosity of the two simulated slurries is significantly higher than corresponding experiments, by a factor of 6 to 10 at larger shear rates.

One has to keep in mind that the error between simulated and experimental viscosity can go up to a factor of 1000. Hence, from the simulation results of the DPP2 model, the DPP2 model was evaluated to be a qualitatively accurate model for viscosity prediction. As previously noted, the relevant shear rates of the battery electrode coating process are around 100 to 1000 s^{-1}

Table 4.8 shows the solid elasticity from experiment and the two models. The elasticity experimental results were obtained as described in Section 3.5. The simulated elasticity of both models were obtained through multiple simulations. The elasticity of the simulated active-free and active-composite solids are 12% and 3% above the experimental values, respectively. As described in Sections 4.7 and 4.8, the simulated elasticity is sensitive to ε_a and $\varepsilon_{c,s}$. Hence, we can match the simulated elasticity to the experimental elasticity quite well by adjusting the ε_a and $\varepsilon_{c,s}$.

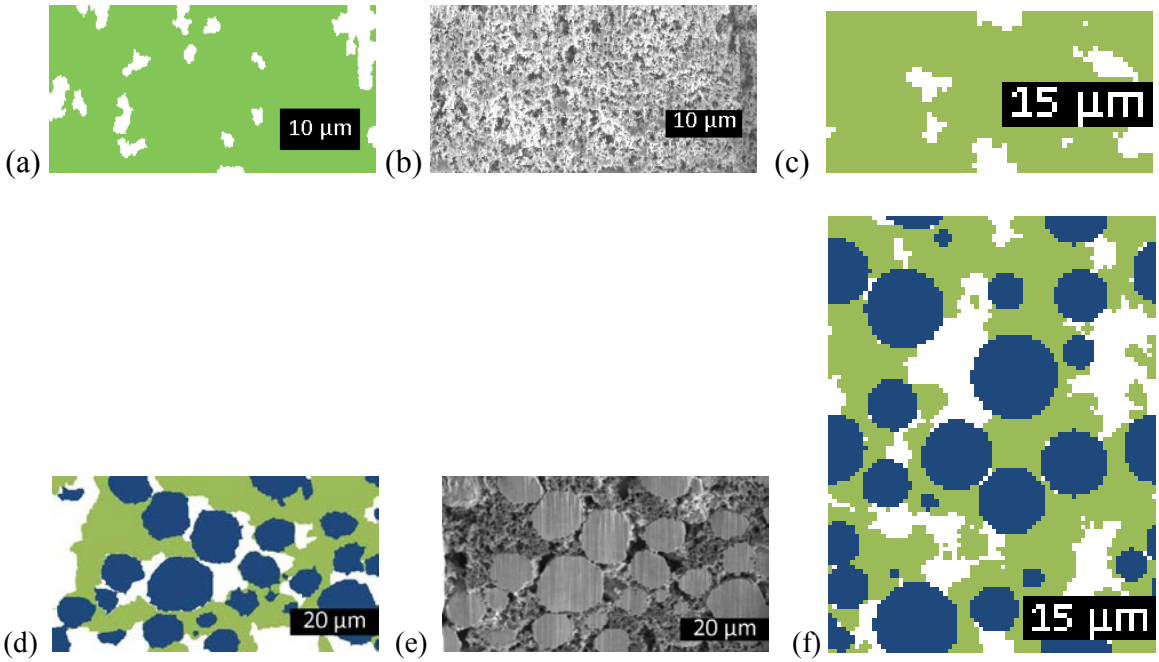

Figure 4.22. 2D cross section images of (a) segmented experimental uncalendered active-free film and (b) unsegmented experimental uncalendered active-free film, and (c) simulated uncalendered active-free film; 2D cross section images of (d) segmented experimental uncalendered cathode and (e) unsegmented experimental uncalendered cathode, and (f) simulated uncalendered cathode.

Table 4.9. Phase volume fraction of uncalendered active-free film, uncalendered cathode, Active-free model, and Active-composite model.

	Uncalendered active-free film	Active-free model	Uncalendered cathode	Active-composite model
Active material			0.399	0.425
Carbon domain	0.904	0.916	0.388	0.358
Macro-pore	0.096	0.084	0.213	0.217

4.10.3 Image comparison and volume fraction

To determine if the DPP2 model generates structure similar to the cathode films, we need to use structural properties to compare. Qualitative image comparisons and volume fraction are first discussed because they are easy to use. Notably the volume fraction of experimental and simulated structures were only obtained from one sample and one simulation. In addition, we

include the drying process of active-free and active-composite models in the discussion to better understand its influence on the structures.

First we compare the active-free model with the active-free film. Figure 4.22 a and c shows the 2D slice images of uncalendered active-free film and simulated microstructure of the active-free model. The macro-pores appear similar in shape and distribution in both images. For the active-free film, macro-pores appear because the solvent evaporates. For the simulation, the drying process shown in Figure 4.12 tells that macro-pores appear because the box shrinks in *z* direction, constraining carbon domain particles to move more in other directions. As for volume fractions shown in Table 4.9, carbon domain and macro-pore volume fractions of active-free model are 1% larger and 10% less than the experimental values, respectively. The result shows that the active-free model can generate a reasonably reliable microstructure. Notably, the amount of the macro-pore volume fraction of active-free film is relatively small, compared to the carbon domains.

Secondly, we compared the active-composite model with the uncalendered cathode. Figure 4.22 d and f shows the 2D slice images of uncalendered cathode and simulated microstructure of the active-composite model. These two images show a similar arrangement of active material particles, in which active material particles are separated from other active material particles. Moreover, the two images show a similar arrangement of macro-pores, in which most macro-pores appear on the surface of active material particles. However, some of macro-pores are much bigger and longer in the model than those found in the experimental cathode. This is because the drying process (Figure 4.19) makes the active material particles come close to carbon domain particles, which causes large attractions between active material particles and carbon domains in the active-composite model.

Table 4.10. Thickness of film for different calendering pressures following relaxation to 1 bar.

Pressure	1 bar (uncalendered)	5 bar	20 bar	50 bar
Height (μm)	51.5	43.3	40.0	40.2

For the volume fraction comparison shown in Table 4.9, active material, macro-pore, and carbon domains are 5% and 0.77% larger, and 5% less than the experimental values, respectively. This indicates the active-composite model can generate a reasonably reliable microstructure.

4.11. Preliminary result of the calendering process in DPP2 model

After the DPP2 model simulated the slurry-coating and drying processes, it was further used to simulate the calendering process. The calendering process was simulated by compressing the simulated solid of DPP2 model in *z* direction under pressure, then recovering pressure to 1bar. This process describes the fact that, in reality, an uncalendered film is compressed under pressure when passing through rollers, after which the pressure goes back to normal after passing through the machine.

Due to the time limit of this project, there was not time to fully determine the value of pressure used during the calendering process. Here, we estimated the pressure to be around 5 to 50 bar. Hence, three different pressures, 5, 20, and 50 bars were used to compress the simulated solid of DPP2 model. The preliminary results are discussed below.

4.11.1 Thickness change

When the DPP2 model simulates the calendering process on the active-composite solid, it is expected that the size of simulated structure decreases under extra pressure and does not go back to the original size when relaxing the pressure. Here we examine the thickness change of the simulated structure after the calendering simulation at different compression pressures, which is shown in Table 4.10 (only the height of the simulated structure is included because the length and width are not changed during the calendering simulation). The thickness or volumes of these simulated structures after calendering decreased by up to 22% from uncalendered structure. This indicates that the compression brings particles closer, causing more attraction between the particles. This additional attraction is capable of retaining some of particles in their new locations when pressure is relaxed.

When we further compared the result at different compression pressures, we found that the difference in the volume of the calendered solid at 20 and 50 bars is 0.6%. This means that a pressure higher than 20 bars may not cause further volume change of the structure.

Table 4.11 Volume fractions for each of 3 domains from experiment and from simulated microstructures of DPP2 model. The simulated structure cover a range of calendering pressures.

Domain	SEM/FIB	Sim uncal	Sim cal 5 bar	Sim cal 20 bar	Sim cal 50 bar
Active	0.526	0.425	0.519	0.561	0.562
Carbon domain	0.358	0.358	0.411	0.426	0.425
Macro-pore	0.116	0.217	0.070	0.013	0.013

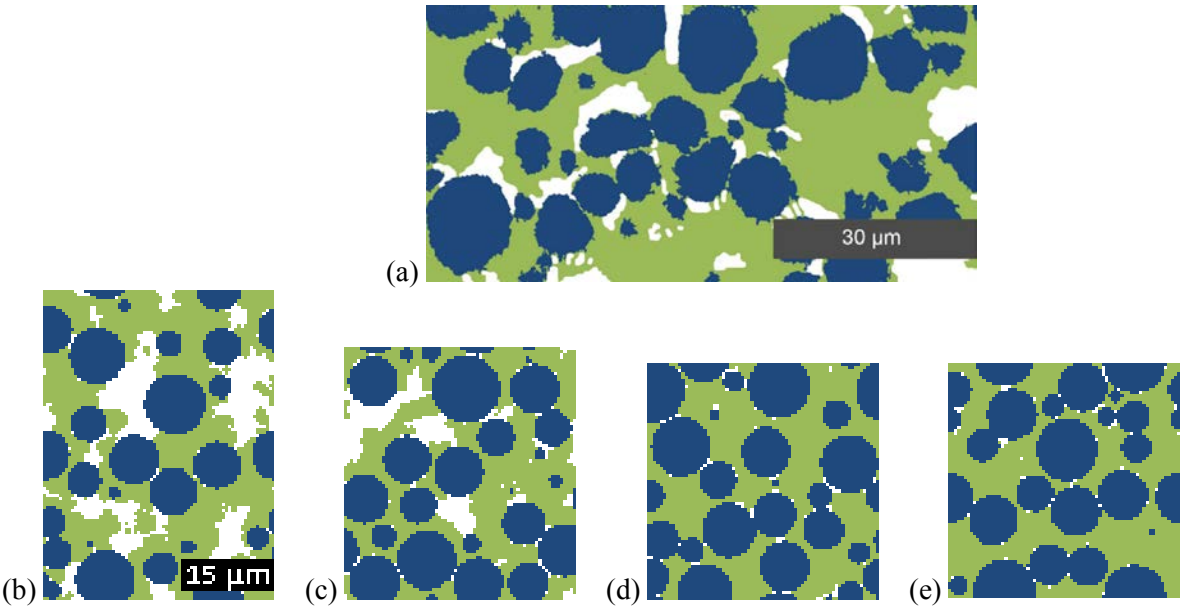

Figure 4.23. 2D cross section images of (a) experimental calendered cathode and (b) simulated calendered cathode, and simulated calendered cathode compressed to (c) 5 bar (d) 20 bar (e) and 50 bar. Parts (c)-(e) have the same scale as parts (a)-(b).

4.11.2 Image comparison and volume fraction

In order to know how well the models simulated calendered structures, qualitative image comparison and volume fraction were used. Figure 4.23 shows 2D cross section images of the calendered cathode, the simulated uncalendered cathode, and the simulated calendered cathode at compression pressures of 5, 20, and 50 bars. All three of the calendered simulated structures have a similar arrangement of active material particles relative to the experimental structure. On the other hand, large-size macro-pores appear most in the first simulated calendered structure compared to the other two simulated structures. These large-size macro-pores are surrounded by the active material particles, which makes it look similar to the experiment structure.

We further examined the difference between the experimental and simulated calendered structures through a volume fraction comparison. As shown in Table 4.11, the active material, macro-pore, and carbon domain volume fractions at a compression pressure of 5 bar are 1% below, 40% below, and 15% above the experimental values, respectively. From Figure 4.23 a

and c, the large difference of macro-pore and carbon domain volume fractions does not significantly change the arrangement of macro-pores, which are surrounded by the active material particles. On the other hand, the active material, macro-pore, and carbon volume fractions at compression pressures 20 and 50 bars are all 6% below, 89% below, and 19% above the experimental values, respectively. It is apparent that the compression of the simulated box during calendering makes the macro-pores disappear, which is reflected by the macro-pore volume fraction difference.

From the above results, the calendering simulation at a compression pressure 5 bar shows the closest match to the experimental calendered structure. However, the experimental compression pressure when an uncalendered cathode passes the rollers is expected to be much higher than 5 bar, based on our experience and confined by Figure 3.6. This indicates that the uncalendered simulated structure is too soft and allows too much plastic deformation at relatively low stress.

This problem can be solved in the future by increasing the stiffness of the particles so that they resist deformation at low compression pressures. First, Using a higher value for K_n can increase the granular potential energy generated when particles are overlapped, which would make the simulated structure stiffer under high pressure. However, this higher K_n can cause the simulated viscosity to become higher than the experimental value. Secondly, using higher K_t can cause more tangential force as particles are overlapped. This tangential force could also make the simulated structure stiffer. Third, increasing $x_{\mu,s}$, the friction factor for solid that controls the upper limit of the tangential force, can also increase the granular restraining force in the DPP2 model. $x_{\mu,s}$ can be set up to the maximum value 1000 instead of the LAMMPS recommended value 1. Notably, changes in σ and ε for active material particles and carbon domain particles

are not considered here since they can change the particles' arrangement in the structure and the film elasticity.

A second observation is that the volume fraction of each phase of the simulated structure at compression pressures of 20 and 50 bars are essentially equal, which indicates that a pressure higher than 20 bars may not cause much more volume change of the structure. This simulation imitated the fact that there is a limit for the thickness change of a sample before the stiffer active material particles make full contact. Experimentally, continued calendering past this point can cause active material particles to crack or to dig into current collector.

4.11.3 Ionic and electronic conductivities

Ionic and electronic conductivities comparison is another way to evaluate the robustness of the DPP2 model in the calendering simulation. As described in Section 3.4.2, the conductivity model uses the finite volume method and periodic boundary conditions to compute the ionic and electronic conductivities of the 3D structures, which makes the conductivity less-dependent on the size of the structure.

Table 4.12 shows the ionic and electronic conductivities of the simulated uncalendered and calendered microstructures of DPP2 model and the experimental calendered microstructure. For ionic conductivity, as expected, the simulated calendered structure at a compression pressure of 5 bar has a smaller value in all directions than the experimental calendered structure, and the simulated calendered structure at compression pressures of 20 and 50 bars have significantly smaller values in all directions than the experimental calendered structure. This indicates that there are fewer pores in these three calendered microstructures for ions to move through, as discussed above. In addition, the simulated uncalendered structure has an ionic conductivity

Table 4.12 Ionic and electronic conductivities of simulated microstructure of DPP1 model and experimental structure of the calendered cathode. z is normal to plane of the film, and it is the direction of drying and calendering.

		SEM/FIB	Sim (uncalendered)	Sim at 5 bar	Sim at 20 bar	Sim at 50 bar
Ionic conductivity ($mS\ cm^{-1}$)	X	42.8	50.1	19.8	11.1	11.4
	Y	26.0	51.4	20.1	11.3	11.6
	Z	28.8	65.0	22.8	10.9	11.0
Electronic conductivity ($mS\ cm^{-1}$)	X	72.6	49.6	84.9	94.2	93.8
	Y	54.8	51.8	84.5	94.8	95.6
	Z	54.5	59.1	91.7	98.2	94.4

significantly higher than the experimental value because of the higher macro-pore volume fraction as shown in Table 4.9. This suggests that a simulated structure with calendering pressure between 1 and 5 bar would reasonably reproduce average experimental ionic conductivity.

When we further examined the ionic conductivity in the x, y, and z directions. The experimental, simulated uncalendered structure, and simulated calendered structure at compression pressure 5 bar show anisotropy, but in different directions. The experimental structure is more conductive in the horizontal (x, y) directions than in the vertical direction (z). The simulated uncalendered structure and simulated calendered structure at compression pressure 5 bar are more conductive in the vertical direction than the horizontal direction. This can be explained by the shape of the macro-pores in the above two simulated structures—they are more elongated in xy plane but thinner in yz and xz planes. This phenomenon is caused by the shrinkage of the simulated box in the z direction during drying and calendering simulations, in which particles fill the holes in the z direction. On the other hand, the simulated calendered structure at compression pressures of 20 and 50 bars do not show much difference in each direction, which indicates that most of the large, irregular shapes of macro-pores do not appear in the structure.

As expected, the electronic conductivity has the opposite results compared to ionic conductivity. The fewer macro-pores contained in the structure, the greater the electronic conductivity it has. The results also show that the simulated calendered structure at compression pressure 5 bar is more conductive in the vertical direction than the horizontal directions. This also corresponds to the fact that there are more particles connected in vertical direction.

The preliminary results for the experimental conductivity of NCM cathode shows that the conductivity is higher in the xy plane, contrary to the simulation result. It is possible that this result is an artifact because the computed experimental conductivity is based on the structure of one sample. If more samples are used the experimental error can be decreased and the resulting conductivity measurement may more closely match the simulation results.

To make the simulated structure more conductive in the x and y directions instead of the z direction, there are possible solutions. For instance, the size change of carbon domain particles from $d_{c,\mathrm{l}}$ to $d_{c,\mathrm{s}}$ can be changed gradually corresponding to real time, instead of instantaneously, during the drying simulation. This can provide enough time for interactions between carbon domain particles and active material particles to make the shapes of macro-pores equilibrated. On the other hand, if we want experimental results to match the simulation results, so that the experimental structure has higher conductivity in the z direction, we can speed up the drying process by using a higher oven temperature to dry the slurry.

4.12. Conclusion

This chapter describes the development of the DPP2 model used to simulate the fabrication of Li-ion electrodes, namely the slurry-coating, drying, and calendering processes. To gain experience in making the DPP2 model, a solid structure simulation model (DPP1) was

developed. LJ/SF potential was used in the DPP1 model to control the interactions between particles. The DPP2 model was later built by using a linear combination of granular-type and LJ/SF potentials.

The DPP2 model was divided into two submodels : active-free and active-composite. Results for both submodels were validated in this chapter. The 2D cross-sectional images of the simulated structure of the models have a particle arrangement similar to the experimental structure. The submodels show reasonable agreement with the experimental values for liquid and solid mass density, shrink ratio, and elasticity. For the viscosity, both models show shear-thinning behavior, which is a characteristic of slurries. The viscosity of both models are considered as semi-quantitative results even the viscosity of the two simulated slurries is significantly higher than the corresponding experiments, by a factor of 6 to 10 at larger shear rates. The volume fractions of the simulated structures of the active-free and active-composite models have better agreement with the experimental values, which is also reflected in the 2D cross sectional images of the structure.

The preliminary result for the calendaring simulation in the DPP2 model shows that the thickness of the simulated structure decreases under extra pressure and does not go back to the original size when the pressure is relaxed. The qualitative image comparisons and volume fraction results show that the calendering simulation at a compression pressure of 5 bar has the closest match to the relative experimental calendered structure, in contrast to the results from the higher compression pressures. However, the exact compression pressure when an uncalendered cathode passes the rollers is expected to be much higher than 5 bar. This discrepancy needs to be resolved by increasing the stiffness of the uncalendered simulated structure.

The conductivity comparison shows that the experimental calendered structure is more conductive in the horizontal (x, y) directions than in the vertical direction (z). The simulated uncalendered and calendered structures at a compression pressure 5 bar are more conductive in the vertical direction than the horizontal direction. On the other hand, the simulated calendered structure at compression pressures of 20 and 50 bars are nearly independent of direction.

In summary, the DPP2 model has the potential to assist in optimizing the microstructure of electrodes. The DPP2 shows the ability to simulate the slurry-coating, drying, and calendaring processes, and it presents qualitative results in simulating liquid and solid behaviors as well as the final solid structure. As long as the calendering simulation can be made to simulate the liquid behavior more reasonably and avoid plastic deformation at low compression pressure, the DPP2 model can be used to further predict electrode performance for different manufacturing and design conditions. For instance, one could examine different component compositions and different slurry-coating speeds and find the optimized microstructure of electrodes to lower transport resistance.

There are a few things can be done to improve the DPP2 model. First, the compression pressure used to compress the uncalendered cathode as it passes through rollers needs to be measured. With the known compression pressure, the DPP2 model can be parameterized to this. Specifically, the uncalendered structure of the DPP2 model needs to be increased in elastic modulus or yield stress to avoid plastic deformation at low compression pressures. The appearance of the plastic deformation caused most of macro-pores in the microstructure to disappear, which does not make it agree with the experimental calendered structure. Second, the DPP2 model can be updated to use irregularly-shaped particles for the active material instead of spherical particles. This can also improve the agreement between the simulated structure and the

experimental structure, after which the ionic and electronic conductivities can be fine-tuned to better match the experimental values.

Bibliography

1. Palaia, J., *Global Battery Market Forecast to Reach USD$144 Billion in 2016*, in *PR Newswire*2012.

2. Linden, D., and Reddy, T. B. , *Batteries Primer*, in *Handbook of Batteries*.

3. *Fuel Properties Comparison*, Alternative Fuels Data Center.

4. *Global Battery Markets*, 2015, Battery University.

5. Goonan, T.G., *Lithium use in batteries.* U.S. Geological Survey Circular, 2012. **1371**.

6. Chakrapani, V., Rusli, F., Filler, M. A., and Kohl, P. A., *A combined photovoltaic and Li ion battery device for continuous energy harvesting and storage.* Journal of Power Sources, 2012. **216**: p. 84-88.

7. Vishkasougheh, H.M., and Tunaboylu, B., *Charactrization of a Li-ion battery based stand-alone a-Si photovoltaic system.* Applied Surface Science, 2014. **318**: p. 324-333.

8. Gering, K.L., Sazhin, S. V., Jamison, D. K., Michelbacher, C. J., Liaw, B. Y., Dubarry, M., and Cugnet, M., *Investigation of path dependence in commercial lithium-ion cells chosen for plug-in hybrid vehicle duty cycle protocols.* Journal of Power Sources, 2011. **196**(7): p. 3395-3403.

9. Hémery, C.-V., Pra, F., Robin, J.-F., and Marty, P., *Experimental performances of a battery thermal management system using a phase change material.* Journal of Power Sources, 2014. **270**: p. 349-358.

10. Shih, Y.-T., Wu, C.-H., Hung, F.-Y., Lui, T.-S., and Chen, L.-H., *A study at room temperature and 55°C on the charge–discharge characteristics of Si(100−x)Alx thin film anode for Li-ion batteries.* Surface and Coatings Technology, 2013. **215**: p. 79-84.

11. Kuo, Y.-C., and Lin, J.-Y., *One-pot sol-gel synthesis of Li4Ti5O12/C anode materials for high-performance Li-ion batteries.* Electrochimica Acta, 2014. **142**: p. 43-50.

12. Ai, W., Luo, Z., Jiang, J., Zhu, J., Du, Z., Fan, Z., Xie, L., Zhang, H., Huang, W., and Yu, T., *Nitrogen and sulfur codoped graphene: multifunctional electrode materials for high-performance li-ion batteries and oxygen reduction reaction.* Adv Mater, 2014. **26**(35): p. 6186-92.

13. Brodd, R.J., and Helou, C., *Cost comparison of producing high-performance Li-ion batteries in the U.S. and in China.* Journal of Power Sources, 2013. **231**: p. 293-300.

14. Singh, D.P., George, A., Kumar, R. V., ten Elshof, J. E., and Wagemaker, M., *Nanostructured TiO2Anatase Micropatterned Three-Dimensional Electrodes for High-Performance Li-Ion Batteries.* The Journal of Physical Chemistry C, 2013. **117**(39): p. 19809-19815.

15. Yi, Y.B., Wang, C. W., and Sastry, A. M., *Compression of Packed Particulate Systems: Simulations and Experiments in Graphitic Li-ion Anodes.* Journal of Engineering Materials and Technology, 2006. **128**(1): p. 73.

16. Wang, C.-W., and Sastry, A. M., *Mesoscale Modeling of a Li-Ion Polymer Cell.* Journal of The Electrochemical Society, 2007. **154**(11): p. A1035.

17. Siddique, N.A., and Liu, F., *Process based reconstruction and simulation of a three-dimensional fuel cell catalyst layer.* Electrochimica Acta, 2010. **55**(19): p. 5357-5366.

18. Smith, M., García, R. E., and Horn, Q. C., *The Effect of Microstructure on the Galvanostatic Discharge of Graphite Anode Electrodes in LiCoO[sub 2]-Based Rocking-Chair Rechargeable Batteries.* Journal of The Electrochemical Society, 2009. **156**(11): p. A896.

19. Wang, Y., Wu, J., and Wei, F., *A treatment method to give separated multi-walled carbon nanotubes with high purity, high crystallization and a large aspect ratio.* Carbon, 2003. **41**(15): p. 2939-2948.

20. Kuroda, S., Tobori, N., Sakuraba, M., and Sato, Y., *Charge–discharge properties of a cathode prepared with ketjen black as the electro-conductive additive in lithium ion batteries.* Journal of Power Sources, 2003. **119-121**: p. 924-928.

21. Wiedemann, A.H., Goldin, G. M., Barnett, S. A., Zhu, H., and Kee, R. J., *Effects of three-dimensional cathode microstructure on the performance of lithium-ion battery cathodes.* Electrochimica Acta, 2013. **88**: p. 580-588.

22. Stephenson, D.E., *Microstructure and Transport Properties of Porous Li-ion Electrodes*, 2011, Brigham Young University

23. Zacharias, N.A., Nevers, D. R., Skelton, C., Knackstedt, K., Stephenson, D. E., Wheeler, D. R.,, *Direct Measurements of Effective Ionic Transport in Porous Li-Ion Electrodes.* Journal of the Electrochemical Society, 2012. **160**(2): p. A306-A311.

24. Stephenson, D.E., Hartman, E. M., Harb, J. N., Wheeler, D. R., *Modeling of Particle-Particle Interactions in Porous Cathodes for Lithium-Ion Batteries.* Journal of The Electrochemical Society, 2007. **154**(12): p. A1146.

25. Stephenson, D.E., Walker, B. C., Skelton, C. B., Gorzkowski, E. P., Rowenhorst, D. J., Wheeler, D. R., *Modeling 3D Microstructure and Ion Transport in Porous Li-Ion Battery Electrodes.* Journal of The Electrochemical Society, 2011. **158**(7): p. A781.

26. Landau, D.P., and Binder K., *A Guide to Monte Carlo Simulations in Statistical Physics, Fourth Edition*. 2014: Cambridge University Press.

27. Steve Plimpton, A.T., Paul Crozier, *LAMMPS Molecular Dynamics Simulator.*

28. Flaim, T., Wang, Y. and Mercado, R., *High Refractive Index Polymer Coatings.* SPIE Proceedings of Optical Systems Design, 2003.

29. *LITHIUM BATTERY*, THE ELECTRIC ENERGY.

30. Hong, J.K., Lee, J. H., and Oh, S. M. , *Effect of carbon additive on electrochemical performance.* Power Sources, 2002. **111**: p. 90.

31. Jache, B.a.A., P., *Use of graphite as a highly reversible electrode with superior cycle life for sodium-ion batteries by making use of co-intercalation phenomena.* Angew Chem Int Ed Engl, 2014. **53**(38): p. 10169-73.

32. NATE. *How Lithium Polymer Batteries are Made*. Available from: https://learn.sparkfun.com/tutorials/how-lithium-polymer-batteries-are-made.

33. Winter, M., and Brodd, R.J., *What Are Batteries, Fuel Cells, and Supercapacitors.* Chemistry Review, 2004(104): p. 4245.

34. Park, M., Zhang, X., Chung, M., Less, G. B., and Sastry, A. M., *A review of conduction phenomena in Li-ion batteries.* Journal of Power Sources, 2010. **195**(24): p. 7904-7929.

35. Nevers, D.R., *The Effect of Carbon Additives on the Microstructure and Performa*, 2013, Brigham Young University.

36. Marc Doyle, J.N., *The use of mathematical modeling in the design of lithium polymer battery systems.* MARC DOYLE and JOHN NEWMAN, 1995. **40**(13-14): p. 2191-2196.

37. Fuller, T.F., Doyle, M. and Newman, J. *Simulation and optimization of the dual lithium ion insertion cell*.

38. Joos, J., Carraro, T., Weber, A., and Ivers-Tiffée, E., *Reconstruction of porous electrodes by FIB/SEM for detailed microstructure modeling.* Journal of Power Sources, 2011. **196**(17): p. 7302-7307.

39. Izzo, J.R., Joshi, A. S., Grew, K. N., Chiu, W. K. S., Tkachuk, A, Wang, S. H., and Yun, W., *Nondestructive Reconstruction and Analysis of SOFC Anodes Using X-ray Computed Tomography at Sub-50nm Resolution.* Journal of The Electrochemical Society, 2008. **155**(5): p. B504.

40. Wilson, J.R., Duong, A. T., Gameiro, M., Chen, H.-Yi, Thornton, K., Mumm, D. R., Barnett, S. A., *Quantitative three-dimensional microstructure of a solid oxide fuel cell cathode.* Electrochemistry Communications, 2009. **11**(5): p. 1052-1056.

41. Awarke, A., Wittler, M., Pischinger, S., Bockstette, J., *A 3D Mesoscale Model of the Collector-Electrode Interface in Li-Ion Batteries.* Journal of The Electrochemical Society, 2012. **159**(6): p. A798.

42. K. Rhazaoui, Q.C., C.S. Adjiman, and N. P. Brandon, *Towards the 3D modeling of the effective conductivity of solid oxide.* Chemical EngineeringScience, 2014. **116**: p. 781.

43. Roberts, S.A., Brunini, V. E., Long, K. N., and Grillet, A. M., *A Framework for Three-Dimensional Mesoscale Modeling of Anisotropic Swelling and Mechanical Deformation in Lithium-Ion Electrodes.* Journal of the Electrochemical Society, 2014. **161**(11): p. F3052-F3059.

44. Hutzenlaub, T., Thiele, S., Paust, N., Spotnitz, R., Zengerle, R., and Walchshofer, C., *Three-dimensional electrochemical Li-ion battery modelling featuring a focused ion-beam/scanning electron microscopy based three-phase reconstruction of a LiCoO2 cathode.* Electrochimica Acta, 2014. **115**: p. 131-139.

45. Peterson, S.W., *The Effect of Microstructure On Transport Properties of Porous El*, 2015, Brigham Young University.

46. J. Banks, J.C., B. Nelson, D. Nicol, *Discrete-Event System Simulation*. 2001: Prentice Hall.

47. Sargent, R.G. <*VERIFICATION AND VALIDATION OF SIMULATION MODELS.pdf*>. in *2011 Winter Simulation Conference*. 2011.

48. Li Xia, K.Q., Yuyan Gao, Xia He, and Fangdong Zhou, *High potential performance of Cerium-doped $LiNiCoMnO_2$ cathode material for Li-ion battery* J. Mater. Sci. , 2015. **50**: p. 2914-2920.

49. Thorat, I.V., Stephenson, D. E., Zacharias, N. A., Zaghib, K., Harb, J. N., and Wheeler, D. R., *Quantifying tortuosity in porous Li-ion battery materials.* Journal of Power Sources, 2009. **188**(2): p. 592-600.

50. Alataş, T., Yılmaz, M., Kök, B. V., Koral, A. f., *Comparison of permanent deformation and fatigue resistance of hot mix asphalts prepared with the same performance grade binders.* Construction and Building Materials, 2012. **30**: p. 66-72.

51. Stephenson, D.E., Master's thesis, Brigham Young University, 2008.

52. Yang, Y., Pakkanen, T. A., and Rowley, R. L. , *NEMD Simulations of Viscosity and Viscosity Index.* International Journal of Thermophysics, 2002. **23**.

53. Torquato, S., *Random Heterogeneous Materials.* 2002.

54. Toxvaerd, S., and Dyre, J. C. , *Communication Shifted forces in molecular dynamics.* The Journal of Chemical Physics, 2011(134).

55. Malek, R.a.M., N. , *Dynamics of Lennard-Jones clusters A characterization of the activation-relaxation technique.* Physical Review 2000. **62**.

56. Rowley, R.L.a.S., J. M., *Molecular dynamics simulation of real-fluid mutual diffusion.* All Faculty Publications, 1989.

57. Vyalov, I., Kiseley, M., Tassaing, T., Soetens, J.C., and Idrissi, A. , *Investigation of the Local Structure in Sub and Supercritical Ammonia Using the Nearest Neighbor Approach.* J. Phys. Chem., 2010. **114**.

58. Burdzy, K., *Brownian Motion and its Applications to Mathematical Analysis*. 2013.

59. Rycroft, C.H., Bazant, M. Z., Grest, G. S., and Landry, J. W., *Dynamics of random packings in granular flow.* Physical Review E, 2006. **73**(5).

60. Brilliantov, N.V., Spahn, F., Hertzsch, J.-M. , and Poschel, T. , *Model for collisions in granular gases.* PHYSICAL REVIEW E, 1996. **53**(5).

61. Silbert, L.E., Grest, G. S., and Plimpton, S. J. , *Granular flow down an inclined plane Bagnold scaling and rheology.* Physical Review E, 2001. **64**(051302).

62. Zhang, H.P., and Makse, H. A. , *Jamming transition in emulsions and granular materials.*

scaling and rheology. Physical Review E, 2001. **64**(051302).